The Thesis Committee for Sarah Bryson Coyle
Certifies that this is the approved version of the following thesis:

Reservoir characterization of the Haynesville Shale, Panola County, Texas using rock physics modeling and partial stack seismic inversion

APPROVED BY
SUPERVISING COMMITTEE:

Supervisor: _____
Kyle T. Spikes

_____
Robert H. Tatham

_____
Mrinal K. Sen

Reservoir characterization of the Haynesville Shale, Panola County, Texas using rock physics modeling and partial stack seismic inversion

by

Sarah Bryson Coyle, B.S.Geo.Sci.

Thesis

Presented to the Faculty of the Graduate School of

The University of Texas at Austin

in Partial Fulfillment

of the Requirements

for the Degree of

Master of Science in Geological Sciences

The University of Texas at Austin

August 2014

Dedication

I dedicate this thesis to my parents, Darcie and George Coyle, and to my sisters, Mary and Carolyn Coyle. Thank you for your love and support. You are my rock.

Acknowledgements

I would like to acknowledge and extend my deepest appreciation to my advisor, Dr. Kyle Spikes. His direction and guidance were essential during this project and his support and friendship have been invaluable to me during both my undergraduate and graduate studies.

I would also like to thank my committee members, Dr. Mrinal Sen and Dr. Robert Tatham, for their advice regarding my research and their feedback on my thesis.

I would like to extend sincere thanks to Thomas Hess for his tireless technical support during this project. I would also like to thank Philip Guerrero for his support, his guidance, and his patience with my endless questions.

Thank you also to Kaushik Bandyopadhyay and Alex Martinez of ExxonMobil for feedback and advice on my research. Thank you to my fellow graduate students, specifically Meijuan Jiang, Alex Lamb, and Russell Carter, for their mentorship during my graduate and undergraduate studies. Thank you to Jacqui Maleski, Qi Ren, Han Liu, Lauren Becker, Elliot Dahl, Karl Oskar Sletten, Makoto Sadahiro, Debanjan Datta, Johnathon Osmond, Aleksandr Montelli and Alex Robson, for their input, discussions, and critical reviews at various stages of this work and for entertaining me for a wonderful 2 years in the geophysics lab. Thank you to Margo and Lucas Grace and to all my colleagues at UT Austin for your friendship and support.

I want to thank Chevron for providing the data used in my research, and extend a special thanks to John Desantis for his feedback during the EDGER forum and for his advice on this project. Thank you to the Reservoir Properties from Seismic group at Chevron for their feedback and advice during my visit. Thank you to Autumn Eakin for

her time and effort in facilitating the use of core data and for her hospitality during my visit.

I would also like to thank Mark Nibbelink for access to the Drillinginfo© database and Hampson-Russell© for access to their software and for enrollment in their Hampson-Russell© training course.

Finally, I would like to thank the EDGER forum. Without this consortium, the access to the knowledge and experience of its members, and the financial support it provides, none of this work would have been possible.

Abstract

Reservoir characterization of the Haynesville Shale, Panola County, Texas using rock physics modeling and partial stack seismic inversion

Sarah Bryson Coyle, M.S.Geo.Sci.

The University of Texas at Austin, 2014

Supervisor: Kyle T. Spikes

This thesis investigates the relationship between elastic properties and rock properties of the Haynesville Shale using rock physics modeling, simultaneous seismic inversion, and grid searching. A workflow is developed in which a rock physics model is built and calibrated to well data in the Haynesville Shale and then applied to 3D seismic inversion data to predict porosity and mineralogy away from the borehole locations. The rock physics model describes the relationship between porosity, mineral composition, pore shape, and elastic stiffness using the anisotropic differential effective medium model. The calibrated rock physics model is used to generate a modeling space representing a range of mineral compositions and porosities with a calibrated mean pore shape. The model space is grid searched using objective functions to select a range of models that describe the inverted P-impedance, S-impedance, and density volumes. The selected models provide a range of possible rock properties (porosity and mineral composition) and an estimate of uncertainty. The mineral properties were mapped in three dimensions within the area of interest using this modeling technique and inversion

workflow. This map of mineral content and porosity can be interpreted to predict the best areas for hydraulic fracturing.

Table of Contents

List of Tables

List of Figures

Chapter 1: Introduction

1.1 Motivation

The increased use of horizontal drilling and hydraulic fracturing has made hydrocarbon production economic from low permeability mudrocks. Formations such as the Haynesville Shale, previously considered only as source rocks, are now produced at large scale as natural gas reservoirs. The rock physics used to characterize traditional reservoirs and the assumptions made in that modeling must be changed and adapted to describe heterogeneous, high clay content, and low permeability unconventional reservoirs. The goal of this work is to model effectively the control of mineralogy and rock fabric of the Haynesville shale on elastic properties such that these properties can be predicted away from the borehole locations by applying the model to impedances and density inverted from 3D seismic data.

1.2 Geologic Background

The Haynesville Shale is an Upper Jurassic organic- and carbonate-rich mudstone deposited in a restricted basin surrounded by carbonate platforms. The mudstones of the Haynesville Shale consist of organic matter, siliceous silt, clay, calcite cements and calcite crystals, and carbonate bioclasts (Hammes et al., 2011). The Haynesville Shale lies conformably beneath the Cotton Valley Group siliciclastics and above the Smackover Formation carbonates. Figure 1.1 shows an idealized stratigraphic column and the extent of the Haynesville relative to state, county, and parish boundaries in northeast Texas and northwest Louisiana.

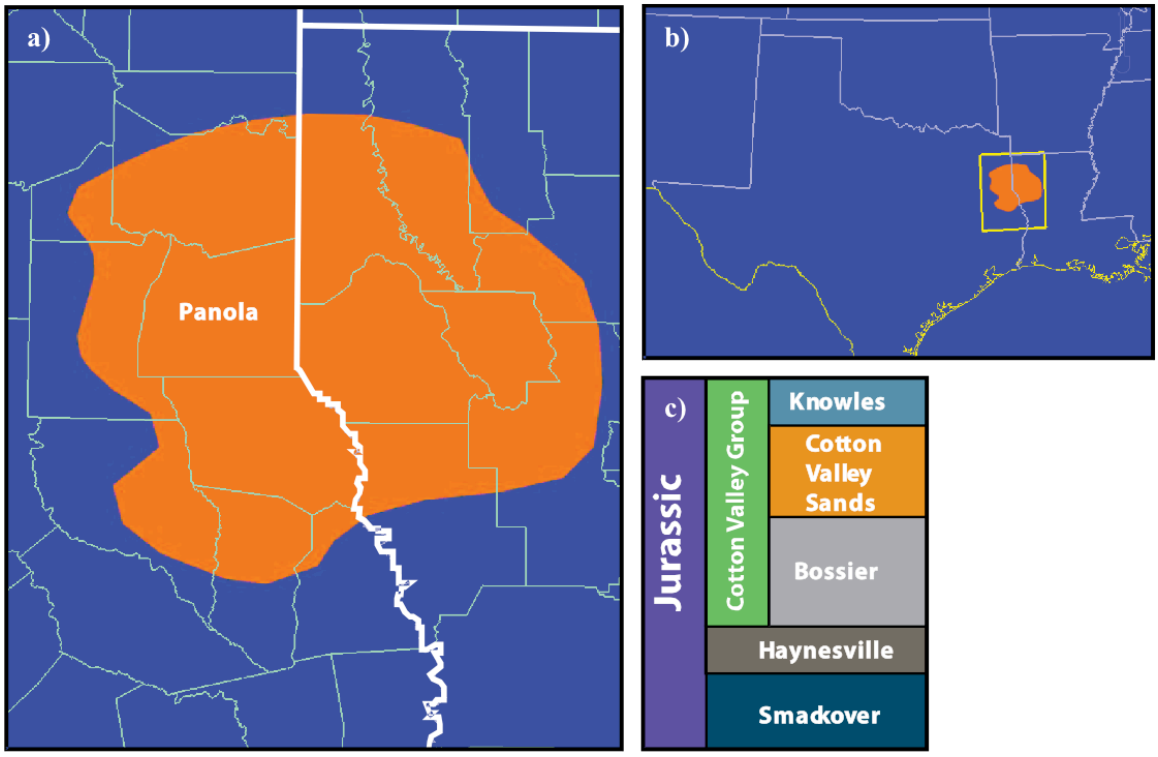

Figure 1.1: a) Map depicting the extent of the Haynesville (orange shaded region) in east Texas and west Louisiana. b) Larger scale map showing location of a) with the yellow rectangle. c) Simplified stratigraphic column showing Haynesville bounded above by Bossier shale and below by the Smackover limestone. (modified from www.eia.gov/oil_gas/rpd/shaleusa4.pdf)

1.2.1 Geologic Setting

The Haynesville Shale was deposited over the Sabine Uplift, a structural high that is part of a broad structural province on the northeastern margin of the greater Gulf of Mexico (GOM) basin. This province extends from east Texas to Florida; the Sabine Uplift is just one structural high block in a series of high and low features in this region associated with opening of the GOM. These features consist of four structural highs with shallow pre-Mesozoic basement and thin Jurassic salt (Sarasota Arch, Middle Ground Arch, Wiggins Uplift and the Sabine Uplift) and five associated pull-apart salt basins (the

Tampa Salt Basin, De Soto Salt Basin, the Mississippi Salt Basin, the North Louisiana Salt Basin, and the East Texas Salt Basin). These blocks controlled the deposition of early Jurassic sediment and salt. This influence continued into the late Jurassic with deposition of Smackover, Haynesville, and Bossier sediments. Figure 1.2 shows the relationship between the Sabine Uplift, the four closest salt basins, and the extent of Haynesville deposition. The southern limit of this Sabine Uplift and Haynesville deposition is marked by the Sabine Island Complex, over which no late Jurassic salt, carbonates, or silicilclastics were deposited (Hammes et al., 2010).

During the time of Haynesville deposition (Kimmergian), a complex system of depositional environments existed in the area of the Sabine uplift. Figure 1.3 shows the paleogeography and spatial relationship of Late Jurassic facies. Carbonate banks and shoals existed encircling the East Texas Salt Basin and at the Southeastern limit of the Sabine uplift (the Sabine Island Complex). Siliciclastic sediment deposition occurred mainly in the East as deltaic deposition with deep-water organic-matter-rich Haynesville shale deposition occurring mainly on the eastern side and crest of Sabine Uplift (Hammes et al., 2010).

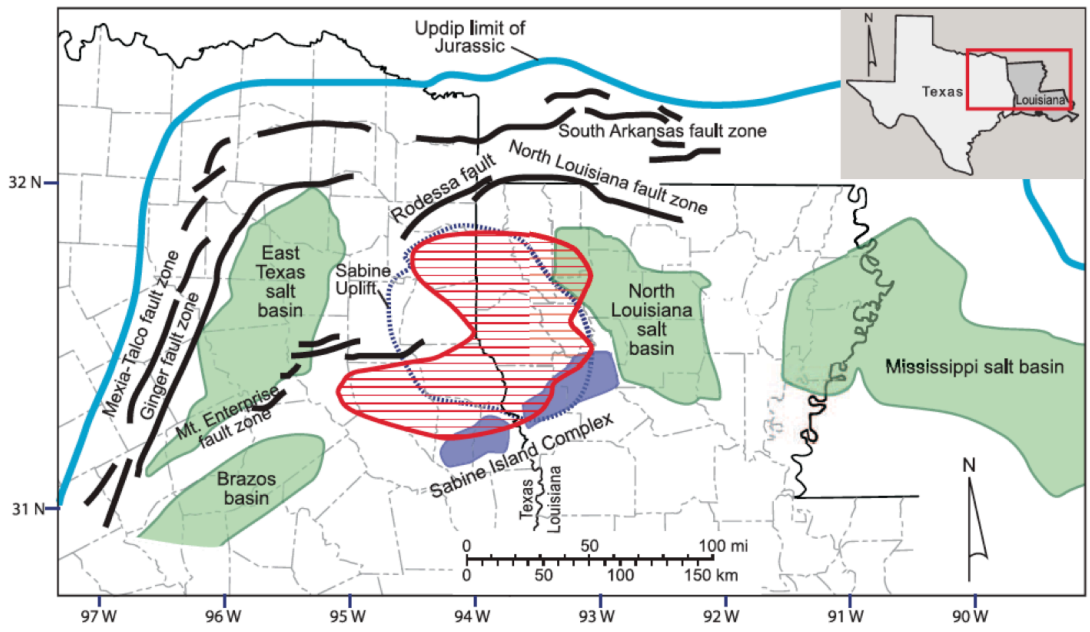

Figure 1.2: Map of the Northeastern Margin of the Gulf of Mexico from Hammes et al. (2010) showing Late Jurassic structural elements and the Haynesville (HVL) Shale productive areas as of 2010. Areas shaded green are basins and areas shaded blue are structural highs. The dashed blue outline shows extent of Sabine uplift. The red striped region shows the eastern depocenter (productive portion) of Haynesville shale.

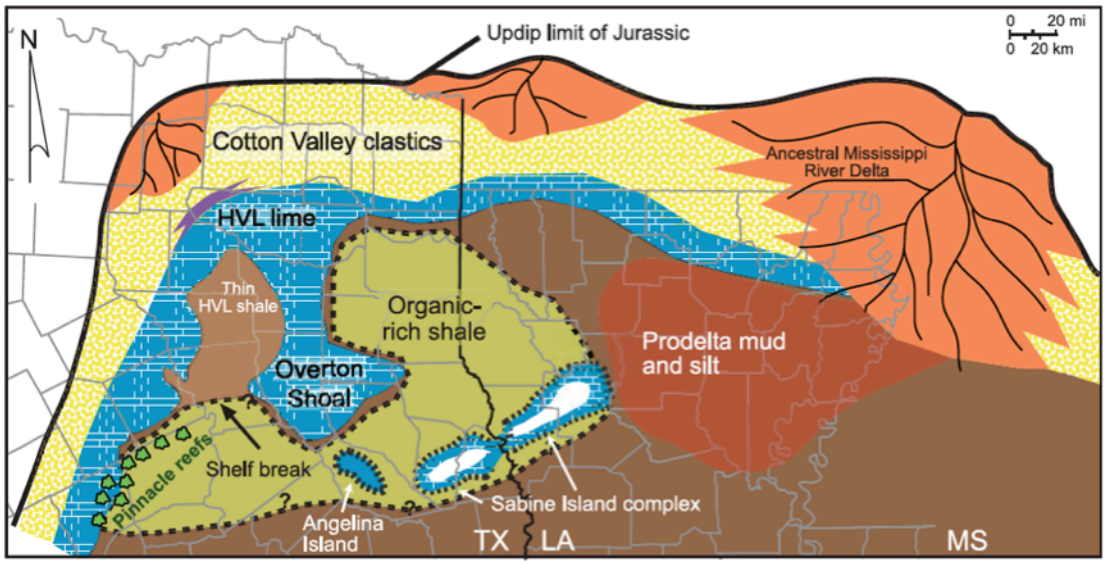

Figure 1.3: Paleogeography of the Northeastern Margin of the Gulf of Mexico from Hammes et al. (2010), showing islands (white), carbonate platforms (blue), Haynesville (HVL) mudstone (green), evaporates (purple), shallow-water clastics (yellow dots), fluvial sediments (light orange), and prodelta (brown) environments.

1.2.2 Regional Geology, Stratigraphy, and Lithofacies

The Smackover Formation carbonates prograded into the basin in an upward-shallowing sequence. With a relative rise in sea level, the carbonates stepped landward. The Haynesville Shale is the basinal equivalent of the transgressive Haynesville Limestone, and the top of the Haynesville Shale is the maximum flooding surface and most landward extent of the second-order transgression and back-stepping of the carbonates. The Haynesville Shale was deposited in two depocenters where there was consistently deeper water: within the East Texas Salt Basin and on the Sabine Uplift. The Sabine Uplift depocenter contains the thicker, shallower, and productive section of the Haynesville, marked in red on figure 1.2. (Hammes et al., 2011). It ranges in depth from

10,500 feet in the northwest to 13,500 feet in this productive depocenter (Buller and Dix, 2009). The Haynesville Shale overlies the Haynesville Limestone in most of this region; however, in the southern-most portion of uplift, the Haynesville limestone pinches out as the Smackover extends further south than overlying transgressive Haynesville (Hammes et al., 2011).

The north-northwest part of the play-area contain a facies with relatively low calcite content, whereas a facies with high calcite content dominates the deeper Haynesville to the south-southeast. Figure 1.4 from Buller and Dix (2009) shows this geometry. Because of this spatial distribution of facies, the carbonate content source was most likely the shallow waters associated with the Sabine Island Complex on the southeast margin of the uplift (Buller and Dix, 2009). However, carbonate content was also contributed from the carbonate ramp crests to north and northwest. Siliciclastic inputs came from deltas north and northeast of the depositional area. Within this larger scale distribution of carbonate and siliciclastic sediment, the calcite and siliciclastic content is also controlled locally by proximity to carbonate buildups (Hammes et al., 2011).

Haynesville mudstones are comprised of clay, organic matter, siliceous silt, calcite cement, carbonate bioclasts, and calcite crtystals. The clay matrix contains illite, mica, chlorite, and kaolinite; the carbonate portion is predominately calcite with some dolomite, ankerite, and siderite. Barite is present as cement; minerals in the siliciclastic fraction are quartz and plagioclase. Pyrite appears throughout Haynesville as concretions, framboids, and as replacement cement (Hammes et al., 2011).

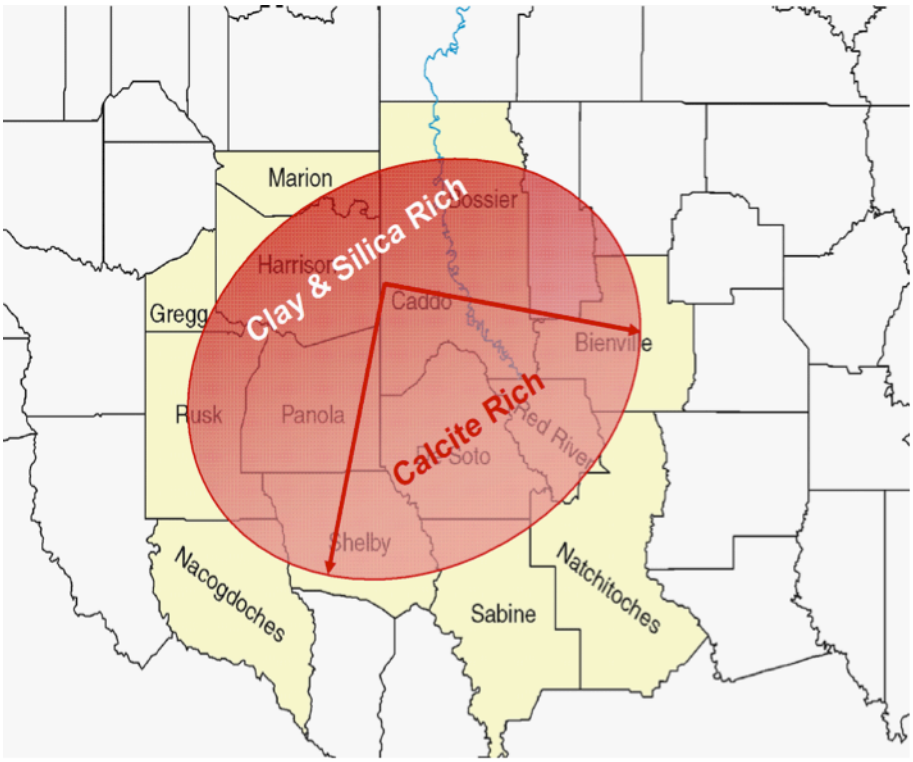

Figure 1.4: Buller and Dix (2009) map illustrates the north-northwest part of the Haynesville's higher concentration of clay and silica, indicated by darker red shading of the oval. To the south-southeast, the lighter shading indicates higher calcite content.

The Haynesville Shale contains three dominant facies: (1) unlaminated peloidal siliceous mudstone, (2) laminated peloidal calcareous or siliceous mudstone, and (3) bioturbated calcareous or siliceous mudstone (Hammes et al., 2011).

(1) The unlaminated peloidal siliceous mudstone is the most organic rich of the facies and contains the most clay content. It is made up of soft peloids, 2-50um in size, that have been reshaped by compaction. This facies tends to be fissile where there is high clay content and massive where there is high carbonate content. The peloidal mudstone contains about 2-6% total organic content (TOC) with the organic matter

randomly dispersed between siliclastic and carbonate grains. It also contains calcite cement layers at bed boundaries as well as fossils including mollusks, brachiopods, and ammonites.

(2) The laminated peloidal facies is the most abundant facies. It contains mm-cm scale laminations of bedding parallel aligned bioclasts, organic layers, peloids, clay, and detridal calcite. It also contains bedding-plane parallel shell layers associated with debris flows and/or turbidity currents, made up of sponge spicules, broken bivalve shells, echinoderm fragments, peloids, and pellets. This facies is more or less carbonaceous or siliciclastic depending on proximity to the source.

(3) The bioturbated mudstone, indicative of oxygenated conditions, occurs at the top of parasequences. This facies also varies in calcareous and siliciclastic constituents based on proximity to source. The burrowers preferentially bioturbated the laminated mudstone facies.

Figure 1.5 shows a photograph, courtesy of Ursula Hammes, of core from Louisiana containing these three facies.

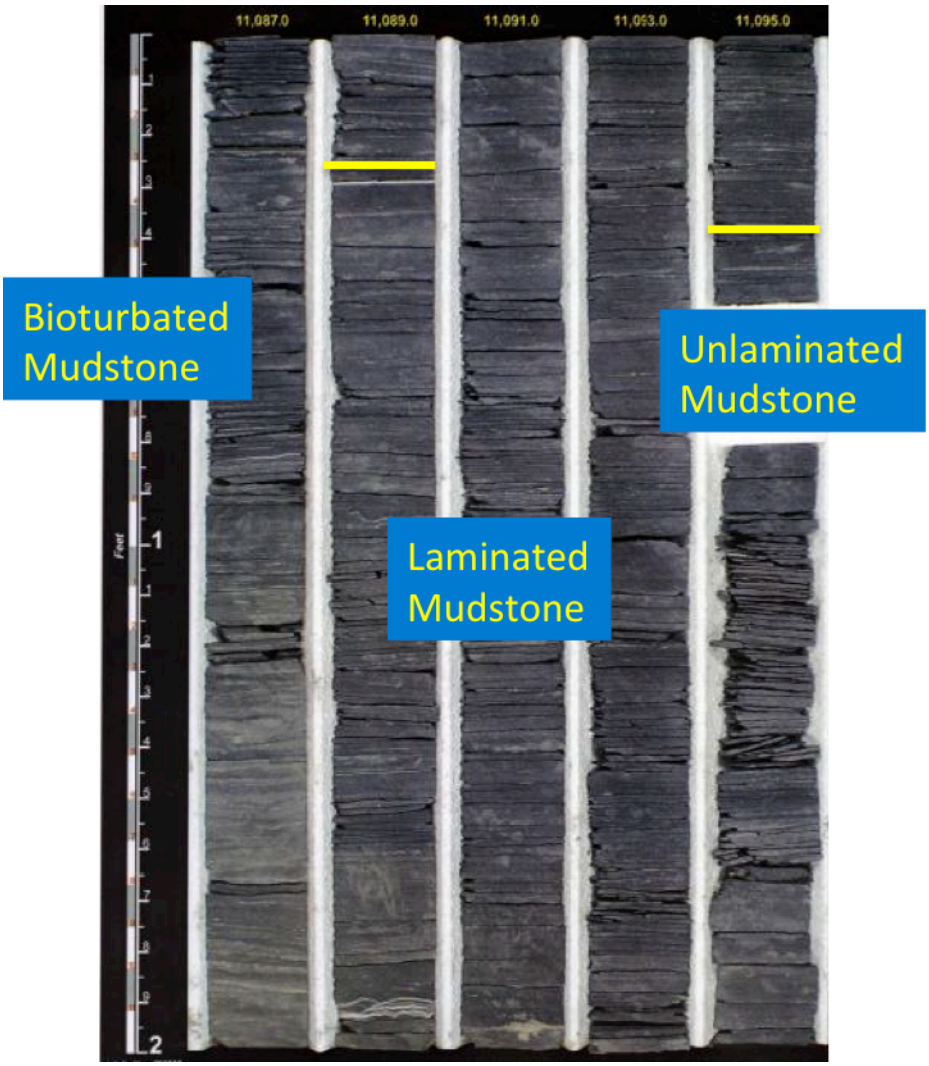

Figure 1.5: Labeled photograph, courtesy of Ursula Hammes, of the three dominant lithofacies (bioturbated mudstone, laminated mudstone, and unlaminated mudstone) within the Haynesville Shale occurring within one core section.

1.2.3 Petrophysics and Production History of the Haynesville Shale

The Haynesville is one of the largest US shale gas reservoirs, with a gas capacity estimated at more than 100 TCF (Hammes et al., 2011). As of December 2010, 1.56 TCF had been extracted from the play. In a period of 3 years, it contributed 60 percent of Louisiana's total gas output. The majority of the abnormally hot and overpressured

Haynesville is thermally mature with only dry gas remaining. The Haynesville Shale has an extremely low permeability, less than 0.001 mD on average, and porosity from about 3 to 14 percent (Wang and Hammes, 2010). The Haynesville typically exhibits vertical transverse isotropy (VTI) at the well log scale (Horne et al., 2012), and both pores and clay platelets tend to align with the bedding orientation at the lab scale (Chalmers et al., 2012). The Haynesville is a very hot and highly overpressured shale with temperatures of over 300F and pressure gradients over 0.9 PSI per foot. This overpressure allows for a very high production initially, as much as 30 mmcf/day, but this initial high production is followed by a steep decline rate. Overpressure was taken into account in the calculation of Haynesville fluid properties (discussed in chapter 3). While it is possible that natural fractures contribute to the rapid decline rate, few open natural fractures have been observed in cores or in imaging logs (Hammes et al., 2011). Thus, vertical natural fractures are considered to be less prevalent in the Haynesville than in other shales (Hammes et al., 2011). Both production successes and challenges are linked to these petrophysical properties and the variable lithofacies.

1.3 PREVIOUS WORK

1.3.1 Rock Physics

Organic-rich shales, like the Haynesville, have very complex rock fabrics. Understanding the grain shapes, pore shapes, and pore networks and the effect of this fabric on bulk elastic properties is important for characterizing the shale from well log and seismic data. Shales are different from sands in more than just mineralogy. Sheet-like clay particles in shales form lower aspect ratio (flatter) pores. Lower aspect ratio pores are more compliant than round pores and reduce the stiffness and the seismic velocity of

the medium. Shales also typically have higher anisotropy due to their preference for aligned orientations of clay particles and clay related-pores during burial and mechanical compaction. Rock physics models are key for linking seismic properties such as P- and S-wave velocity, Vp/Vs, impedance, and elastic moduli to reservoir properties like composition, sorting, lithology, porosity, and fluid saturation. Many different rock physics models are available to characterize this relationship, but to be useful for modeling shales, they must be able to incorporate complex mineralogy and geometry as well as anisotropy.

Empirical models can be used to extrapolate reservoir properties away from well locations once they are carefully calibrated with existing data from the area. Well-known examples of empirical models include velocity-porosity equations by Han (1986), Gardner et al. (1974) velocity-density relations, and Greenberg-Castagna (1992) Vp/Vs equations. In traditional sandstone reservoirs constrained by well log data, these relationships can be useful. However, because shale behavior varies so widely, it is difficult to develop an empirical model that can be extended to multiple shales.

A number of theoretical models approximate the rock as elastic (or in some, poroelastic or viscoelastic) materials. Mixing laws like the Voigt-Reuss or Hashin-Shtrikman (1963) bounds represent the limits on behavior of a two phase elastic composite at all concentrations. While they are too broad for use alone in this work, they are useful in ensuring that other theoretical elastic models remain physically reasonable.

Contact models of clastic rocks approximate the rock volume as individual grains such that the nature of the grain-to-grain contact determines the elastic properties. Most of these are based on the Hertz-Mindlin (Mindlin, 1949) description of elastic response of two adjacent spheres (Avseth et al., 2010). Although these models are very useful for

describing cementation in traditional reservoirs, they do not easily allow for the variety in grain and pore shape that inclusion models do.

Most inclusion models represent the medium as an elastic solid with idealized ellipsoidal or penny shaped cavities, the compliance of which is determined by pore shape. Kuster and Toksöz (1974) provide a long-wavelength first order scattering theory to approximate both P- and S-velocities that can account for different inclusion shapes (Kuster and Toksöz, 1974; Berryman, 1980). This model, however, cannot account for a large concentration of inclusions while still honoring the Hashin-Strikman bounds. The self-consistent approximation (SCA) accommodates a higher volume of inclusions by describing the deformations of the inclusions without defining the initial host material. Similarly the differential effective medium model (DEM) allows for a high concentration of inclusions, but unlike the SCA, the DEM establishes a host or framework material into which inclusions are added (Budiansky, 1965; Hill, 1965; Wu, 1966). In this way, a mineral can be treated as connected or load-bearing even at low concentrations (Montaut, 2012). This is untrue of the SCA in which a material is connected only at volumes of 40–60% (Berryman, 1980).

Though the application of rock physics models to shales is still fairly young, multiple studies have been done to adapt traditional models to represent heterogeneity, complex mineralogy and grain shapes, and anisotropy of shales. Hornby et al. (1994) combines the SCA and the DEM model in order to combine phases that contribute equally as background materials and the order dependent differential effective medium model to add remaining mineral phases. Vernik and Landis (1996) use a modified version of the Backus average to model anisotropy of organic rich shales. Bandyopadhyay (2009) models the anisotropy of the same dataset as Vernik and Landis

using the anisotropic DEM with kerogen as the background material. Ruud et al. (2003) and Draege et al. (2006) provide rock physics models to describe the change in elastic properties of shales with compaction. Ruud's model relates all seismically observable properties, P- and S-velocities, and the three anisotropic parameters of a transversely isotropic medium, to silt content and porosity. Draege (2006), like Hornby (1994), combines the SCA and the DEM model to represent a shale at different stages in mechanical and chemical compaction. Jiang (2014) combines Chapman's (2003) model for cracks and the self consistent model to represent the shapes of pores, cracks, and fractures within the Haynesville Shale.

In order to incorporate both the effect that pore and grain shapes have on rock stiffness and the resulting anisotropy, this thesis employs the anisotropic DEM. The anisotropic DEM can be used to build complex mineralogy and rock fabric by iteratively adding both mineral and pore space inclusions as idealized ellipsoids. It describes changes in shape of these inclusions as changes in aspect ratio (the ratio between the shortest and longest axes of the inclusion). This is a great simplification of the complex grain and pore shapes present within shales. However, with this simplification, the model still describes the effect of inclusion shape on stiffness and on anisotropy, while allowing inclusion shape to be described with only one parameter, aspect ratio.

1.3.2 Seismic Inversion

Quantitative interpretation of seismic amplitudes can be used to estimate rock properties away from the borehole. In heterogeneous shale reservoirs, this seismic characterization is important for identifying the best locations for production. Many previous methodologies for characterizing shale reservoirs from seismic data are intended to investigate the presence of natural fractures. Such work predominantly uses

discontinuity attributes (semblance or coherence) or uses azimuthal variations of the velocity or the impedance field (e.g., Zhang et al., 2010). Other seismic characterizations of shales are designed to describe the "brittleness" of the shale. This is often done through inversion for Poisson's ratio and Young's modulus as a proxy, respectively, for "fracability" and TOC volume and porosity. Rickman et al. (2008) showed that the "brittleness" of a rock formation can be predicted from Poisson's ratio and Young's modulus. Alzate and Devegowda (2013) demonstrate a methodology for using an inversion of seismic data for Young's modulus and Poisson's ratio along with production data to predict whether regions of the Lower Barnet Shale will be good, intermediate, or poor areas from which to produce. Alzate and Devegowda's (2013) method assumes that a high inverted Poisson's ratio indicates a more ductile shale interval. This technique also assumes an inverse relationship between Young's modulus and porosity, TOC, and clay content in soft sedimentary rocks. This relationship was documented in several shales using nano-indentation tests by Kumar et al. (2012). However, application of a more rigorous rock physics model is necessary for a detailed characterization of shale composition. Jiang (2014) uses Chapman's (2003) model for cracks in conjunction with the SCA to invert 3D seismic impedance volumes to give a more detailed characterization of porosity, pore shape, and mineral assemblage. In this thesis, I use the anisotropic DEM with the same grid searching technique as Jiang (2014) to describe changes in composition and porosity throughout the Haynesville Shale.

1.4 Outline of Thesis

Chapter 1 describes the geologic background of the Haynesville Shale, including the environment of deposition/ geologic setting, the regional geography and stratigtaphy, the lithofacies of the Haynesville, and the production history and petrophysics. Previous

rock physics work for conventional and unconventional reservoirs and previous seismic characterization of shales are discussed. Chapter 2 introduces the study area and dataset. The data includes prestack and poststack seismic data from a 3D seismic survey, well log data from 2 vertical wells, geophysical measurements from core, as well as images from the core. Chapter 3 reviews important geophysical fundamentals and describes methods used in this thesis for determining mineral and fluid properties, effective medium modeling, model-based simultaneous impedance inversion, and grid searching. It includes an explanation of the anisotropic DEM model, its formulation, and rock typing. Chapter 4 describes the rock physics modeling characterization of the relationship between elastic and reservoir properties of the Haynesville. It discusses calibration results and final results of the modeling. Chapter 5 describes the grid searching, impedance inversion, and rock physics inversion and results. Chapter 6 includes conclusions drawn from previous chapters and makes recommendations for future work.

1.5 REFERENCES

Avseth, P., T. Mukerji, G. Mavko, and J. Dvorkin, 2010, Rock-physics diagnostics of depositional texture, diagenetic alterations, and reservoir heterogeneity in high-porosity siliclastic sediments and rocks – A review of selected models and suggested work flows: Geophysics, **75**, 5, 75A31–75A47.

Alzate, J. H., and D. Devegowda, 2013, Investigation of surface seismic, microseismic, and production logs for shale gas characterization: Methodology and field application: Interpretation, **1**, 37–49.

Bandyopadhyay, K., 2009, Seismic anisotropy: geological causes and its implications to reservoir geophysics: Ph.D. thesis, Stanford University.

Berryman, J. G., 1980, Long-wavelength propagation in composite elastic media: The Journal of the Acoustical Society of America, **68**, 1809–1831, doi: 10.1121/1.385171.

Budiansky, B., 1965, On the elastic moduli of some heterogeneous materials: Journal of the Mechanics and Physics of Solids, **13**, 223–227.

Buller, D., and M. C. Dix, 2009, Petrophysical evaluation ofthe Haynesville Shale in northwest Louisiana and northeast Texas: Gulf Coast Geological Association of Geological Societies Transactions, **59**, 127**–**143.

Chalmers, G. R., R. M. Bustin, and I. M. Power, 2012, Characterization of gas shale pore systems by porosimetry, pycnometry, surface area, and field emission scanningelectron microscopy/transmission electron microscopy image analyses: Examples from the Barnett, Woodford, Haynesville, Marcellus, and Doig units: AAPG Bulletin, **96**, 1099–1119, doi: 10.1306/10171111052.

Chapman, M., 2003, Frequency-dependent anisotropy due to meso-scale fractures in the presence of equant porosity: Geophysical Prospecting, **51**, 369–379.

Dræge, A., M. Jakobsen, and T. A. Johansen, 2006, Rock physics modeling of shale diagenesis: Petroleum Geoscience, **12**, no. 1, 49–57, doi: 10.1144/1354-079305-665.

Gardner, G. H. F., L. W. Gardner, and A. R. Gregory, 1974, Formation velocity and density—The diagnostic basics for stratigraphic traps: Geophysics, **39**, 770–780, doi: 10.1190/1.1440465.

Greenberg, M. L., and J. P. Castagna, 1992, Shear-wave velocity estimation in porous rocks: Theoretical formulation, preliminary verification and applications: Geophysical Prospecting: **40**, 2, 195–209, doi: 10.1111/j.1365-2478.1992.tb00371.x.

Hammes, U., H. S. Hamlin, and R. Eastwood, 2010, Facies characteristics, depositional environments, and petrophysical characteristics of the Haynesville and Bossier shale gas plays of east Texas and northwest Louisiana: Houston Geological Society Bulletin, May 2010, 59-63.

Hammes, U., H. S. Hamlin, and T. E. Ewing, 2011, Geologic analysis of the Upper Jurassic Haynesville Shale in east Texas and west Louisiana: AAPG Bulletin, **95**, 10, 1643–1666.

Han, D., 1986, Effects of porosity and clay content on acoustic properties of sandstones and unconsolidated sediments: Ph.D. dissertation, Stanford University.

Hashin, Z., and S. Shtrikman, 1963, A variational approach to the elastic behavior of multiphase materials: Journal of the Mechanics and Physics of Solids, **11**, 2, 127–140, doi: 10.1016/0022-5096_63_90060-7.

Haynesville-Bossier Shale Play, Texas-Louisiana Salt Basin. 26 May 2011. Web. 1 Aug. 2013. <http://www.eia.gov/oil_gas/rpd/shaleusa4.pdf>.

Hill, R., 1965, A self-consistent mechanics of composite materials: Journal of the Mechanics and Physics of Solids, **13**, 213–222.

Hornby, B., L. M. Schwartz, and J. A. Hudson, 1994, Anisotropic effective–medium modeling of the elastic properties of shales: Geophysics, 59, 1570–1583.

Horne, S., J. Walsh, and D. Miller, 2012, Elastic anisotropy in the Haynesville Shale from dipole sonic data: First Break, **30**, 37–41.

Jiang, M., 2014, Seismic Reservoir Characterization of the Haynesville Shale: rock-physics modeling, prestack seismic inversion and grid searching: PhD thesis, The University of Texas at Austin.

Kumar, V., C. H. Sondergeld, and C. S. Rai, 2012, Nano to macro mechanical characterization of shale: Annual Technical Conference and Exhibition, SPE, Paper SPE 159808-PP.

Kuster, G. T., and M. N. Toksöz, 1974, Velocity and attenuation of seismic waves in two-phase media, Part I: Theoretical formulations: Geophysics, **39**, 587–606, doi: 10.1190/1.1440450.

Mindlin, R. D., 1949, Compliance of elastic bodies in contact: Journal of Applied Mechanics, **16**, 259–268.

Montaut, A., 2012, Detection and quantification of rock physics properties for improved hydraulic fracturing in hydrocarbon-bearing shales: M.S. Thesis, The University of Texas at Austin.

Rickman, R., M. Mullen, E. Petre, B. Grieser, and D. Kundert, 2008, A practical use of shale petrophysics for stimulation design optimization: All shale plays are not clones of the Barnett Shale: Annual Technical Conference and Exhibition, Society of Petroleum Engineers, SPE 11528.

Ruud, B., M. Jakobsen, and T. A. Johansen, 2003, Seismic properties of shales during compaction: 73rd Annual International Meeting, SEG, Expanded Abstracts, 1294–1297, doi: 10.1190/1.1817522.

Vernik, L., and C., Landis, 1996, Elastic anisotropy of source rocks: Implication for hydrocarbon generation and primary migration: AAPG Bulletin, **80**, 531–544.

Wang, F. P., and U. Hammes, 2010, Effects of reservoir factors on Haynesville fluid flow and production: World Oil, **231**, D3–D6.

Wu, T. T., 1966, The effect of inclusion shape on the elastic moduli of a two-phase material: International Journal of Solids and Structure, **2**, 1-8.

Zhang, K., B. Zhang, J. T. Kwiatkowski, and K. J. Marfurt, 2010, Seismic azimuthal impedance anisotropy in the Barnett Shale: 80th Annual International Meeting, SEG, Expanded Abstracts, 273–277.

Chapter 2: Well and Seismic Data

2.1 Dataset Overview

The dataset used in this thesis is comprised of a 3D seismic volume (both prestack and poststack) and a full suite of well logs from each of 2 vertical wells (referred to here as well A and well B). The relative location within the seismic volume of wells A and B is shown in figure 2.1. The exact geographic location of the survey is considered confidential by the operator. Also used in this work are core data from well B comprised of core description made by the author, photographs of the core made by the author, XRD data and SEM images. The seismic volume, well logs, XRD data, SEM images, and access to the core were all provided by Chevron.

2.2 Well Data

2.2.1 Geophysical Log Data

A full suite of logs, shown in depth, from well A and well B in Panola County were used in this study. In well A, only 900 feet were logged, including 400 feet of Bossier, about 200 feet of Haynesville Shale, and about 300 feet of the underlying Haynesville Limestone. In well B, 10,600 feet were logged including about 100 feet of Haynesville Limestone, about 200 feet of Haynesville Shale, the entire 500 feet of Bossier Shale, and about 9,800 feet of other overlying formations. The full suite of log measurements included resistivity, caliper, gamma ray (GR), neutron porosity (Nphi), density, spontaneous potential, vertical P-wave (Vp) and vertical S-wave (Vs) velocities at both wells. Figure 2.2 and 2.3 show five of these logs with the Haynesville Shale for well A and B, respectively.

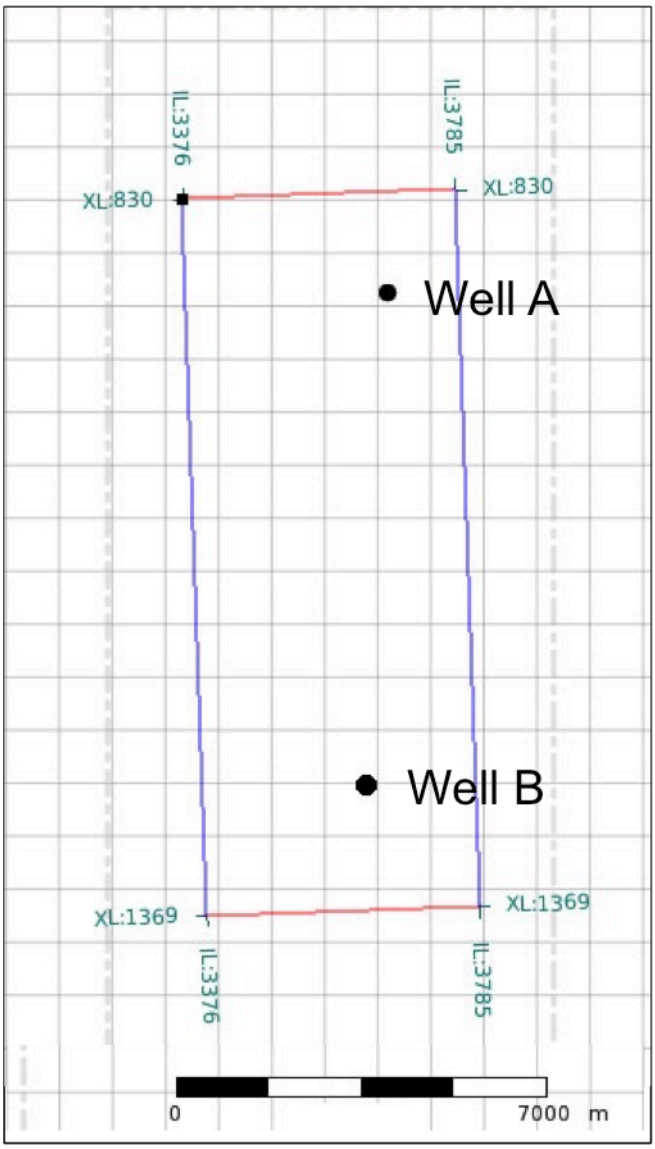

Figure 2.1: Seismic data coverage is indicated by red (extent of crosslines) and blue (extent of inlines) lines labeled with inline and crossline numbers. The entire area of the seismic volume is about 68.83 km^2 . The relative locations of well A and well B are indicated by correspondingly labeled points.

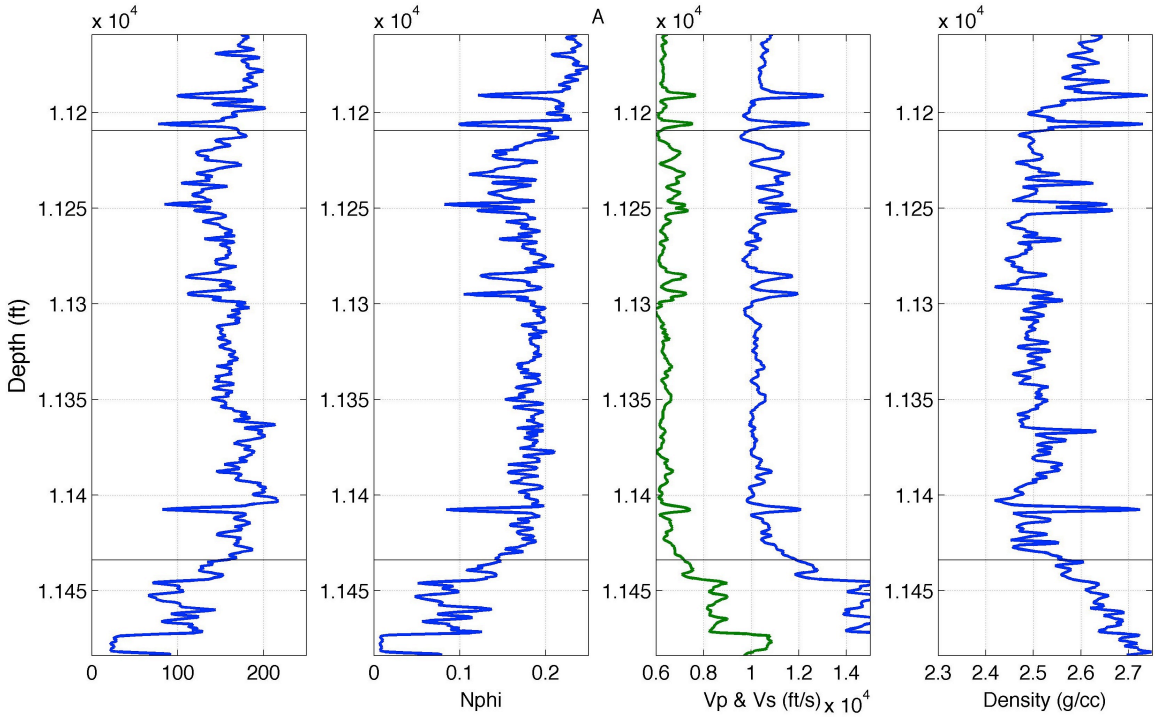

Figure 2.2: Four panels containing five well logs from well A. From left to right they are gamma ray (GR), neutron porosity (Nphi,) S-wave velocity (Vs), P-wave velocity (Vp), and bulk density. The horizontal lines represent the top and base of the Haynesville Shale.

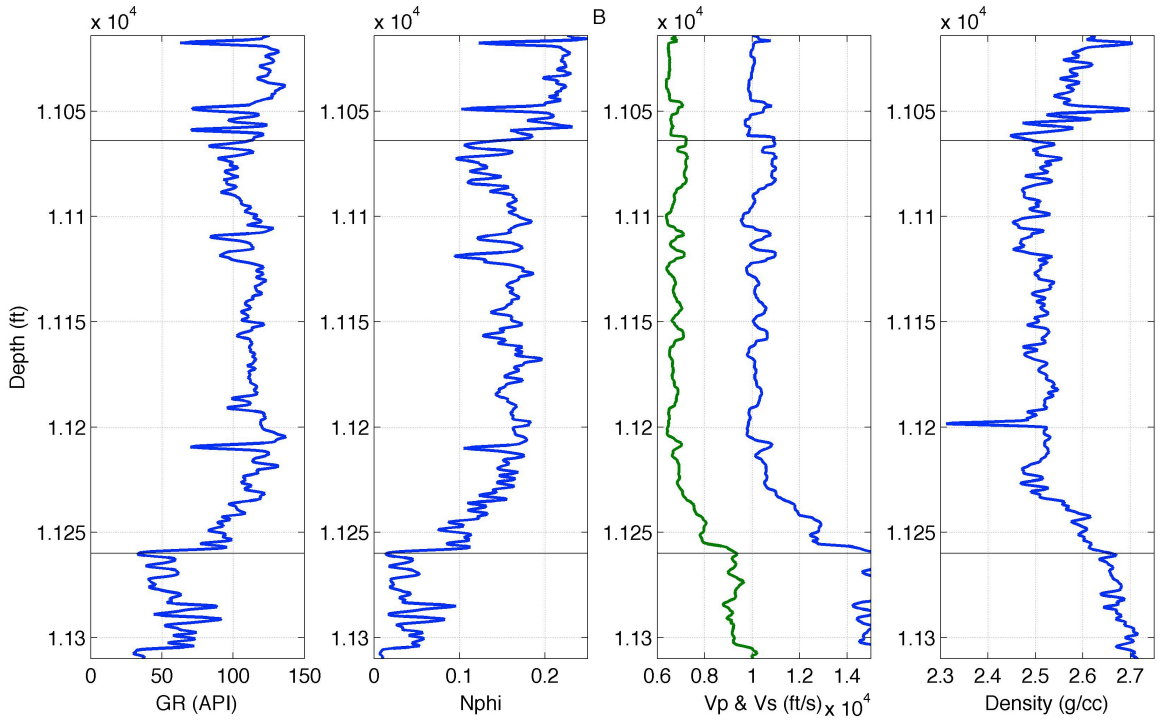

Figure 2.3: Four panels containing five well logs from well B. From left to right they are gamma ray (GR), neutron porosity (Nphi), S-wave velocity (Vs), P-wave velocity (Vp), and bulk density. The horizontal lines represent the top and base of the Haynesville Shale.

Within the Haynesville the Vp ranges from about 10,000 to 12,000 feet per second, Vs from 6,000 to 8,000 feet per second, and density from 2.3 to 2.8 g/cm^3. In both wells, Vp and Vs are well correlated and fairly consistently anti-correlated with GR. The horizontal lines indicate the top and base of the Haynesville Shale. The top of the Haynesville is identified by an increase in both neutron porosity and density logs. This increase in the overlying Bossier indicates a decrease in kerogen and an increase in siliciclastics (Hammes et al., 2011). The base of the Haynesville shows a marked increase in density, Vp, Vs, along with a decrease in GR and neutron porosity in the underlying limestone.

Within the Haynesville, the same trends can be observed in logs from both wells. A higher Vp and Vs can be observed at the top of the Haynesville. This increase in velocity occurs as large spikes in velocity with a corresponding increase in density and corresponding decreases in the GR and Nphi. The evaluation of mineralogical data within the Haynesville illustrates that these spikes are representative of a higher calcite content in the top portion of the Haynesville Shale. Both wells also contain the two spikes in the Vp and Vs curves, the "rabbit ears", that are often used as a distinguishing feature of the Haynesville. Again, these spikes correspond with sharp decreases in GR and neutron porosity increase in density. These ears mark the base of the more calcite rich upper portion of the Haynesville, and the remainder of the log contains a lower Vp and Vs until a large spike near the base of the Haynesville. Beneath this spike, Vp, Vs, and density gradually increase into the underlying limestone as the GR and Nphi gradually decrease.

2.2.2 Core Data

Cores and core measurements were taken from both wells used in this project. From well A, X-ray Diffraction (XRD) mineral volumes were available. From well B, XRD data, scanning electron microscope (SEM) images were available, in addition to GR log measured on the core. The core GR log at well B was compared with the down hole GR measurements from the Haynesville to compensate for error in depth measurement between the core and the borehole. Figure 2.4 shows this comparison and the corresponding adjustment made to the depths of the core measurements. Access was granted to core from well B, and both core descriptions and photographs of the core samples were also used in the project. The cored portion of well B begins at 11,114 feet depth (depth adjusted as described above). The uppermost calcite-rich portion of the Haynesville was not cored at well B. Figure 2.5 contains three photographs and two

SEM images of the core with examples of features described in the Haynesville at well B. The Haynesville at this location is a dark gray fossiliferous mudstone containing silt-sized silica and carbonate grains and carbonate shell hash. It contains both unlaminated to finely laminated facies and varies in fossil content. There are several intervals with increased volume of shell hash; these are likely representative of storm events (figure 2.5b). The majority of the section contains abundant Inoceramus shell fragments (figure 2.5b). The laminated intervals are more heavily bioturbated, though there are some burrows, often replaced by pyrite, in unlaminated intervals (figure 2.5a). Several vertical calcite-filled fractures are present in the core (figure 2.5c), but no open fractures were identified. The lowermost portion of the Haynesville becomes gradationally lighter in color with depth. Comparison with XRD measurements confirms that this color change is indicative of an increase in calcite content. The base of the Haynesville is readily apparent as the rock becomes much more calcareous. SEM images were taken throughout the cored section. Figure 2.5d provides an example of a calcite grain (top arrow) and of a pyrite framboid (lowermost arrow). Figure 2.5e contains an SEM image of compacted aligned clay flocculates.

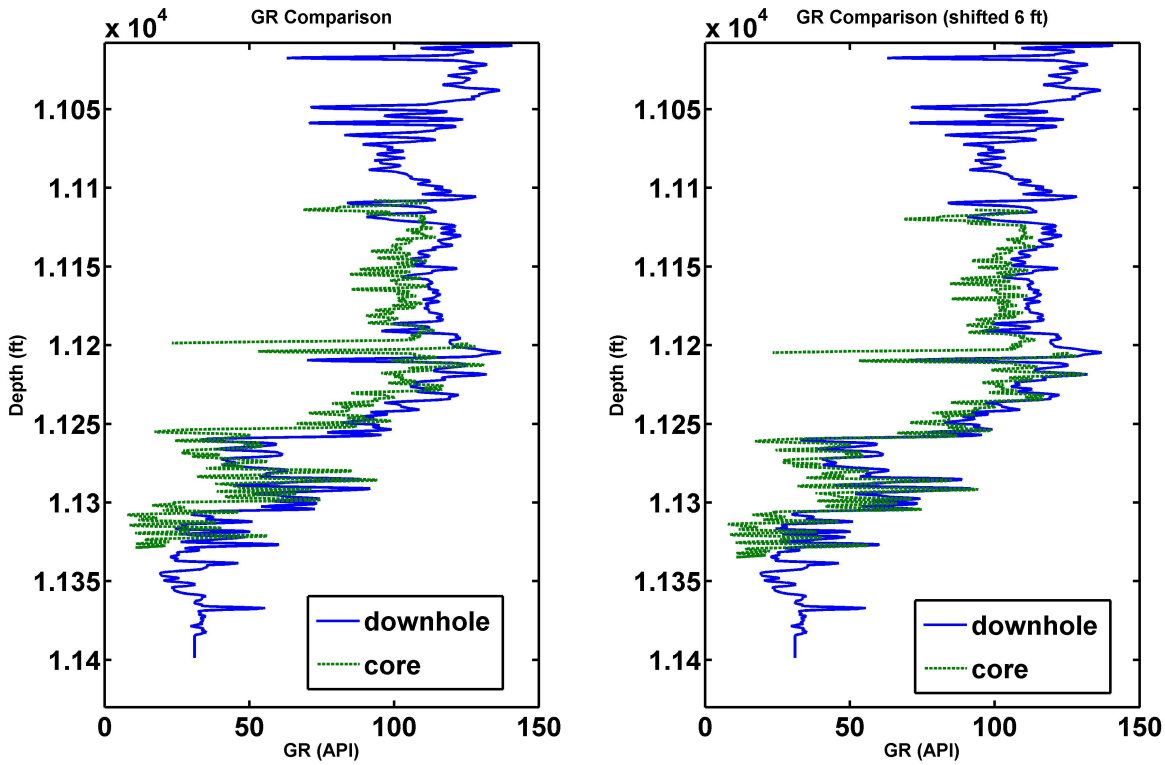

Figure 2.4: Two log panels each showing a comparison between gamma ray measured in the bore hole (blue solid) and gamma ray measured from the core (green dashed). The panel on the left shows GR against the measured depth. The panel on the right depicts the same but with a 6 foot shift applied to the core such that features in both logs correlate in depth.

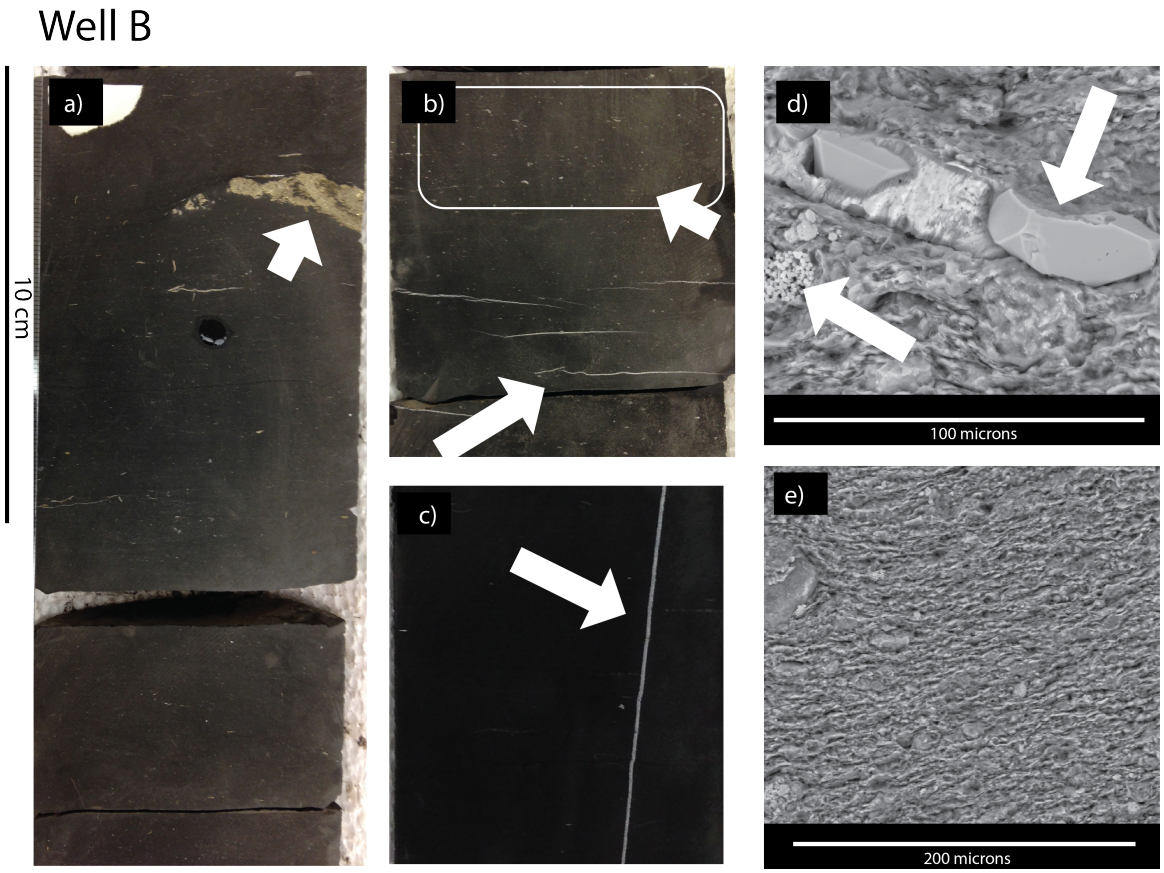

Figure 2.5: Well B core photographs and SEM images. The scale bar on the left provides scale for images a) through c). SEM images in d) and e) contain separate scale bars. a) umlaminated dark gray Haynesville mudstone with the arrow indicating a pyrite filled burrow. b) The uppermost arrow and box indicate an interval with increased shell hash. The lowermost arrow identifies an Incoceramus shell. c) The arrow identifies a calcite filled sub-vertical fracture. d) The uppermost arrow indicates calcite, and the lower left arrow indicates a pyrite framboid. e) aligned clay floculates.

2.2.3 Mineralogical Data

Hammes et al. (2011) find that the clay mineral fraction of the Haynesville is comprised predominantly of illite and mica with small amounts of chlorite and kaolinite.

The carbonate content is mostly calcite with minor amounts of dolomite, ankerite, and siderite. The siliciclastic minerals are predominantly quartz, plagioclase and minor amounts of potassium-feldspar (Hammes et al., 2011).

X-ray Diffraction (XRD) data are available from core taken within the Haynesville at 17 different depth points from well A and at 33 depth points in well B. Comparison of XRD mineralogy with ECS logs (as well as previous mineral studies by Hammes et al. (2011) described above) suggests that the ECS mineral phases consist of multiple minerals. Specifically, quartz also includes potassium and plagioclase feldspars, calcite includes dolomite, pyrite includes marcasite, and clay encompasses illite, smectite, mica, and chlorite. The kerogen phase in the ECS logs contains only kerogen. Table 2.1 shows the minerals reported in the ECS logs and in the XRD results. Figure 2.6a and b shows these mineral concentrations with depth at both wells. The inputs to the rock physics modeling done in this work are simplified to the five minerals detected with the ECS logs: quartz, pyrite, calcite, clay and kerogen. The distributions of these minerals are shown in the histograms of figure 2.6b. However, the presence of higher density minerals in the Haynesville, such as dolomite and chlorite, was taken into account in the initial porosity calculations.

Measurement	Mineralogy				
ECS Logs	Quartz	Calcite	Pyrite	Clay	Kerogen
XRD Result	Quartz K-Feldspar Plagioclase	Calcite Dolomite	Pyrite Marcasite	Illite Smectite Chlorite	Kerogen

Table 2.1: XRD vs. ECS – mineral phases table

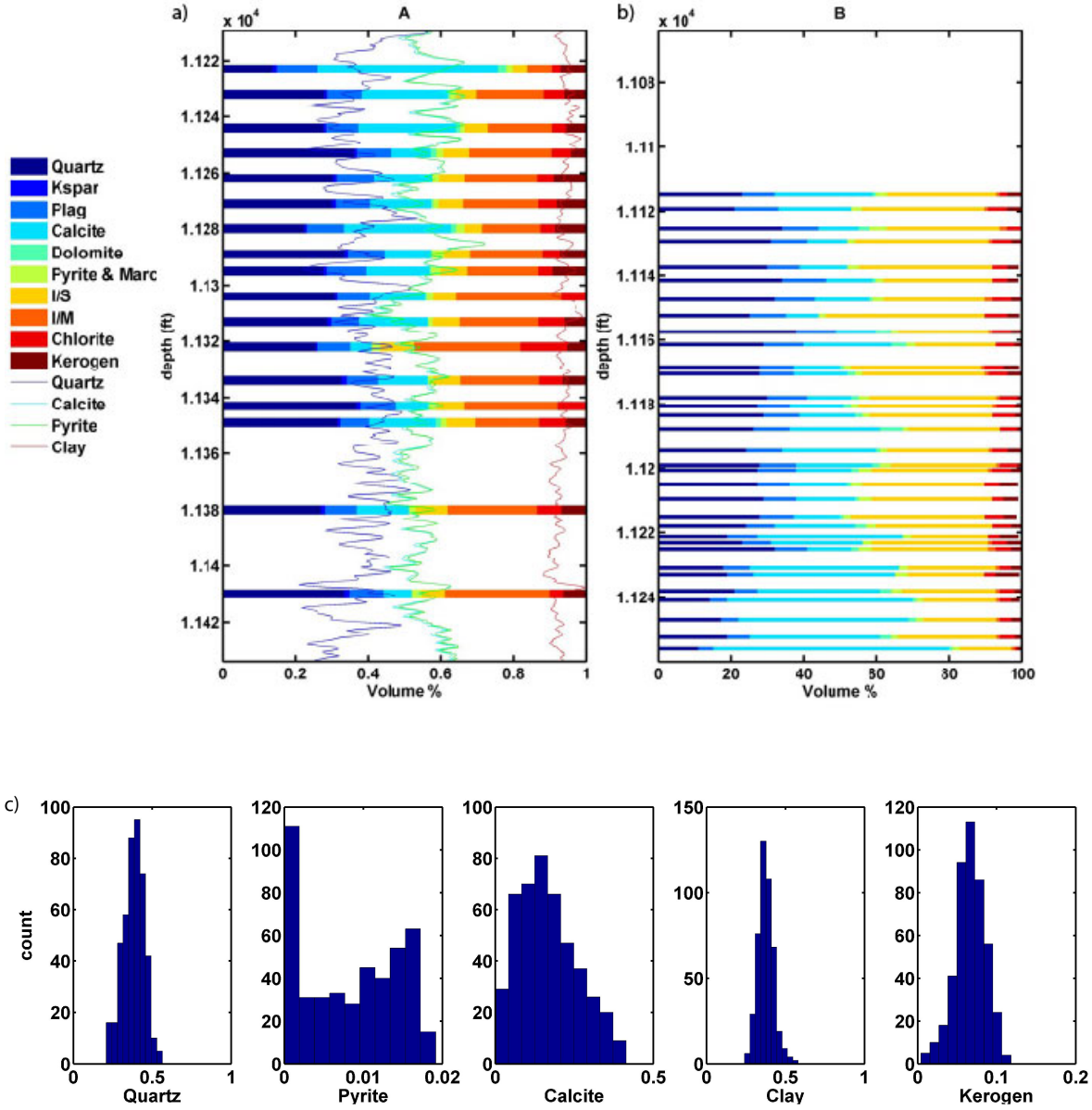

Figure 2.6: Colored bars in a) and b) show the XRD mineral volumes of well A and well B respectively. Both of these panels are in depth and the y axis contains the full Haynesville thickness. Portions without mineral information are regions without XRD data. Colored lines in a) show the corresponding ECS measurements for the 5 mineral phases. c) contains histograms for 5 mineral phases used in modeling from ECS logs from the Haynesville.

The core taken at well B (and thus the XRD data measured from that core) was not taken over the entire length of the Haynesville. However, by comparing the mineral points measured both through XRD and ECS, we can observe similar trends in mineralogy at both wells. High calcite concentration and lower quartz and clay concentration can be seen in both ECS and XRD measurements at the top of well A. Lower calcite and higher clay and quartz volumes can be observed in both A and B in the middle and lower portion of the Haynesville, and an increase in calcite can be observed in both wells nearing the base of the Haynesville. These trends, when compared with the well logs in figures 2.2 and 2.3, show (as expected) a decrease in GR and an increase in velocity and density with increases in calcite relative to quartz and clay. Figure 2.7 contains cross plots of the volumes of these three minerals. In the first two plots, both quartz and clay show strong anti-correlation with calcite. In the third cross plot, quartz versus clay, quartz and clay show no obvious correlation.

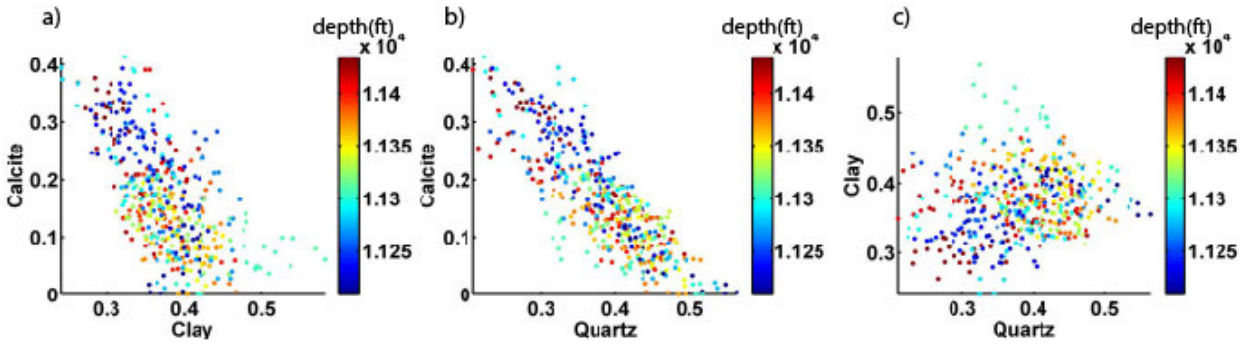

Figure 2.7: Cross plots, colored by depth, of three main minerals in the Haynesville. Both quartz and clay show strong anti-correlation with calcite. Quartz and clay show no obvious correlation with each other.

2.3 SEISMIC DATA

2.3.1 Poststack Data and Horizons

The seismic data (pre- and post-stack) available for this work is a portion of a larger seismic survey. The volume used in this project has an area of about 68.83 km^2 with 409 crosslines and 539 inlines (Figure 2.1). The processed inline spacing is 12.5 m and the crossline spacing is 25 m. The bin size is about 12.5 by 25 m with average fold of 77. Figure 2.8 shows a portion of an inline section in the area of interest through the poststack seismic data in time (ms) with P-wave velocity log measured at well B superimposed in red. The Haynesville Shale is shaded green. The base of the Haynesville Shale is a consistently strong positive reflection, easily identifiable throughout volume. The top of the Haynesville is marked by a trough that varies in amplitude throughout the volume and is not always easy to identify. Reflectivity within the Haynesville also varies throughout the volume. The horizons marking the top and base of the Haynesville used in this project were interpreted on the poststack volume, and NMO corrections were made using this velocity volume from Chevron (Figure 2.9). However, the poststack data does not correlate with the reflectivity predicted by synthetics from the wells. Because the post-stack volume was processed for structural interpretation, the amplitude information was not preserved. Therefore, only the pre-stack volume was used in this work. Horizons from the poststack and the velocity volume associated with its processing were used in this project along with the prestack volume.

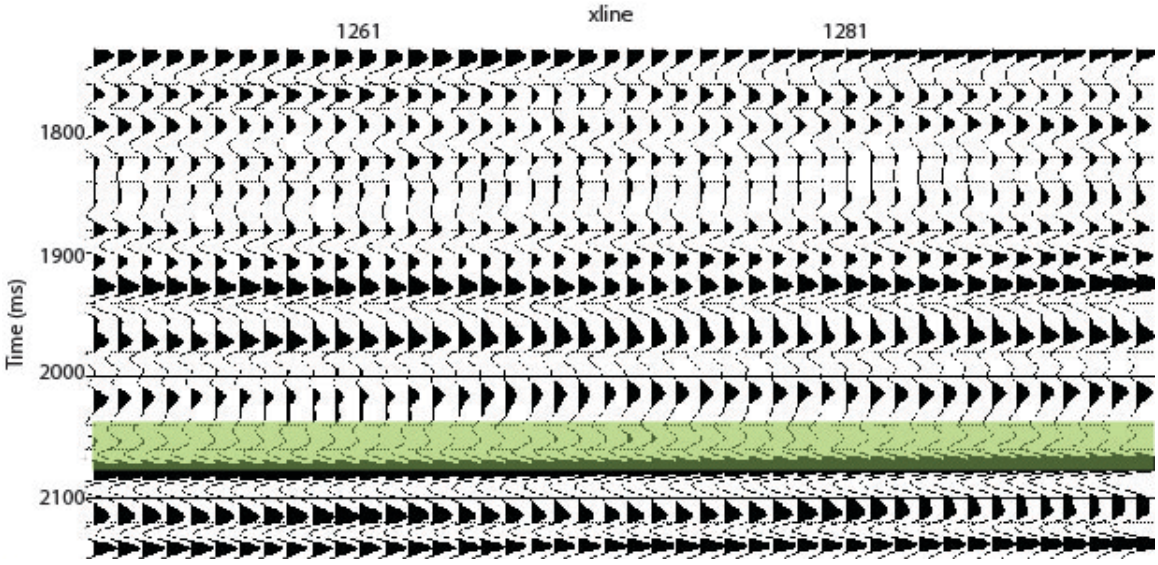

Figure 2.8: Post-stack partial time section from inline 3622. Xline numbers are indicated across the x-axis while time is on the y-axis in ms. The interval of interest, the Haynesville Shale, is highlighted in green.

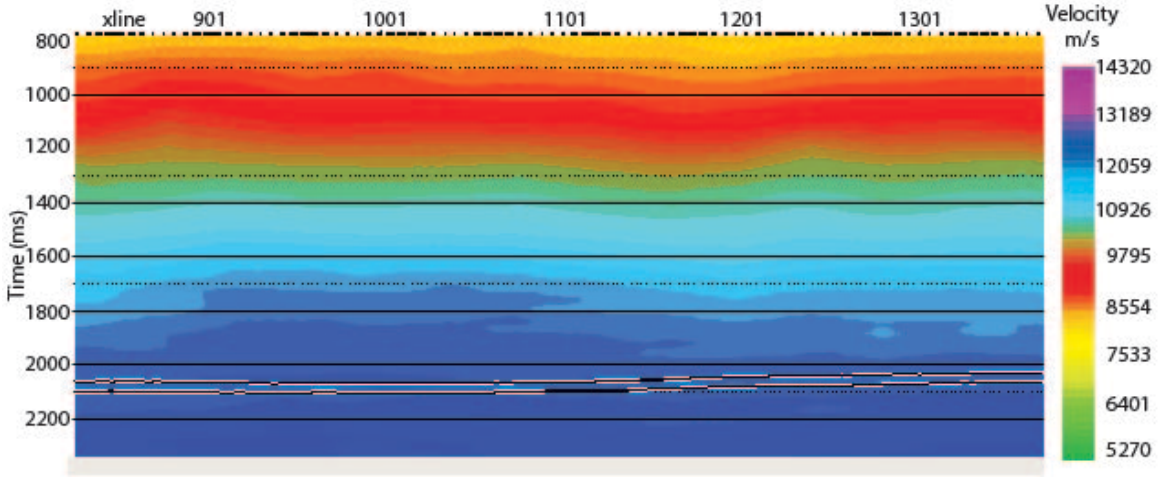

Figure 2.9: Partial section from inline 3622 of the processing velocity volume. Xline numbers are indicated across the x-axis, and time is on the y-axis in ms. The top and base of the interval of interest, the Haynesville Shale, are marked in indicated with red horizons.

2.3.2 Prestack Data

The prestack volume has the same geometry as described above for the poststack data. Offsets range from 225 to 6025 meters allowing for angles from a couple degrees to about 60 degrees. Maximum incidence angles at the top of the Haynesville are about 48 degrees. The survey was shot with vibroseis, dynamite, and air gun (in lakes) with a receiver group of 6 vertical geophones in a 6 foot circular array and with hydrophones. The data were processed by CGG Veritas in June 2011. The data were demultiplexed, trace muted, and edited. A system-dependent gain correction was applied to account for geometric spreading. High amplitude noise-burst attenuation and high amplitude despiking were applied in the shot domain. Surface consistent spike deconvolution with .1 % prewhitening was applied. Preliminary velocity analysis was done followed by an initial surface-consistent residual statics correction. A second pass velocity analysis was performed. Surface-consistent gain corrections, noise-burst attenuation, adaptive linear noise attenuation, radon linear noise attenuation, and source and system phase matching were performed. Next, a second pass of surface consistent residual statics was applied. F-X random noise attenuation was performed. Gabor (1946) spectral whitening and F-X cross-spread random noise attenuation were applied. Trace-by-trace gain was applied with a window of 500-4500 ms. Prestack velocity analysis and Kirchhoff prestack time migration were performed. Finally, acquisition footprint attenuation and residual velocity adjustment were performed.

An example of the prestack seismic data is shown in figure 2.10. A CDP gather from crossline 1274 is shown at inline 3622. The Haynesville is highlighted in green. This pre-stack data still shows considerable coherent noise including multiples that were not removed in the previous processing. I processed the data further using commercial

Hampson-Russell© software to remove these multiples showing residual moveout present in the data. I picked and applied a mute to eliminate shallow noise at far offsets. Incident angles were calculated using the processing velocity volume described above and angle gathers were generated. A parabolic radon random noise suppression filter and a parabolic radon demultiple suppression filter were applied to the entire volume. Figure 2.11 shows an example of a resulting angle gather with the Haynesville again highlighted in green. The coherent noise has been reduced, and the events appear flat even at large angles. Figure 2.12 shows the amplitude spectrum extracted from inline 3622 in the time window 1500 ms to 2200 ms from the processed prestack volume. The frequency range is about 8 to 55 Hz with a dominant frequency of about 25 Hz. If we assume an average p-wave velocity of about 3km/s, the wavelength would be about 120m. Therefore vertical resolution of the seismic data, one fourth of the wavelength, is about 30m.

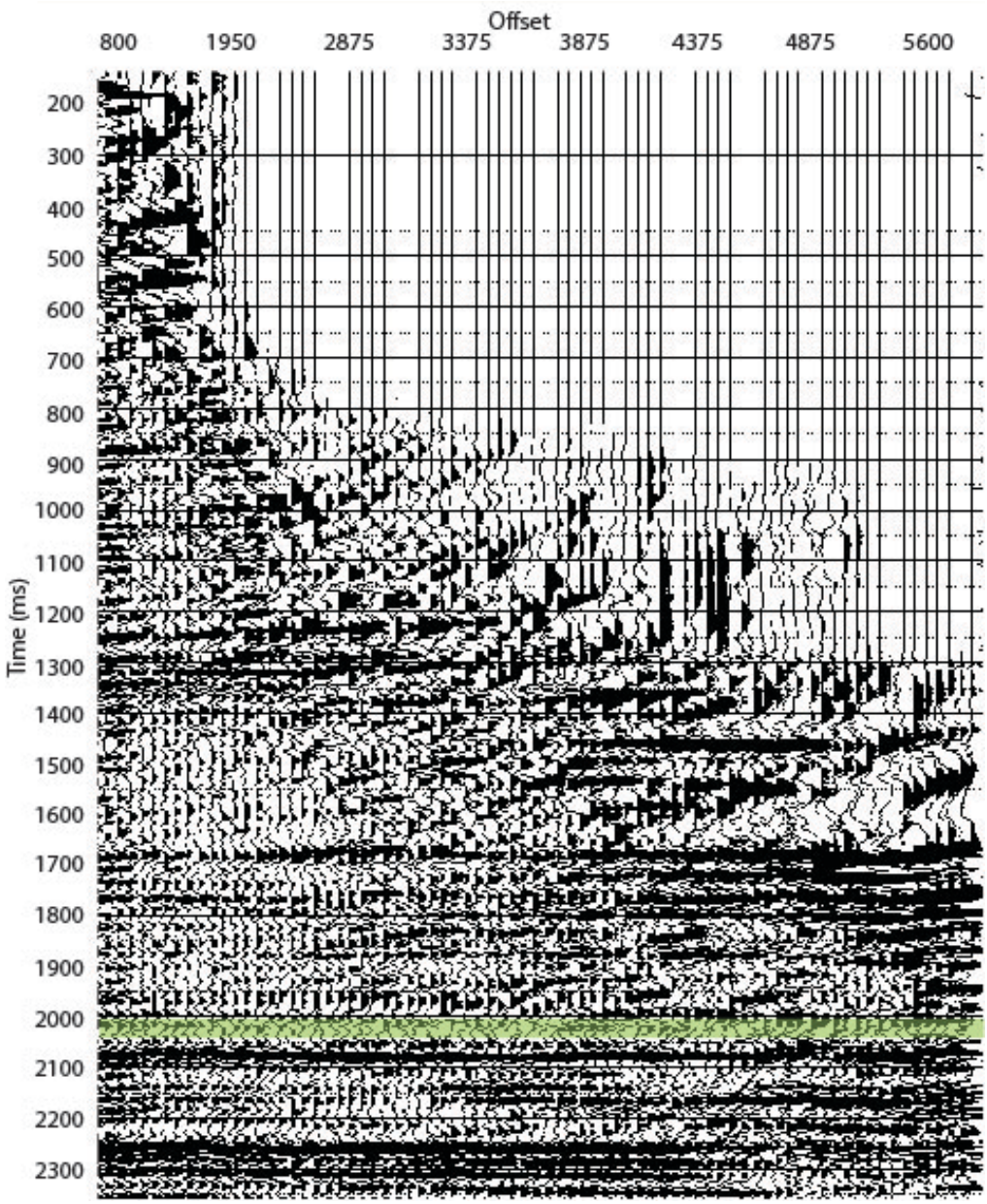

Figure 2.10: An example of the Kirchoff migrated prestack seismic data CDP gathers from crossline 1274 at inline 3622. The Haynesville Shale is highlighted in green.

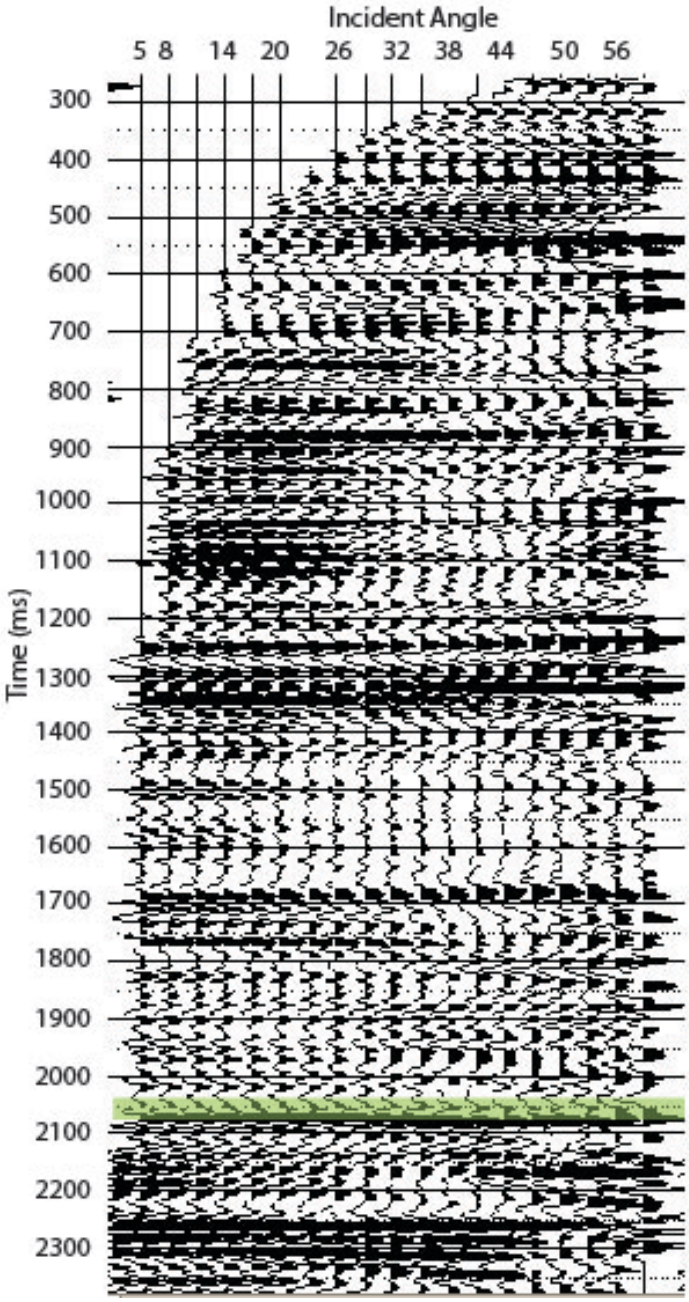

Figure 2.11: An example of a the angle gathers reprocessed by the author from crossline location 1274 at inline location 3622. The Haynesville Shale is highlighted in green.

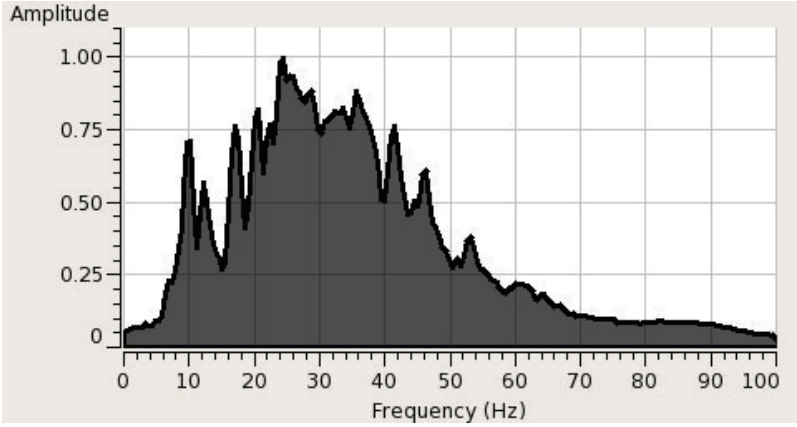

Figure 2.12: Amplitude spectrum extracted from inline 3622 in the time window 1500 ms to 2200 ms from the final processed prestack volume. The dominant frequency is about 25 hz.

2.4 REFERENCES

Gabor, D., 1946, Theory of communication: J. IEEE (London), **93**(III), 429-457.

Hammes, U., H. S. Hamlin, and T. E. Ewing, 2011, Geologic analysis of the Upper Jurassic Haynesville Shale in east Texas and west Louisiana: AAPG Bulletin, **95**, 10, 1643–1666.

Chapter 3: Theory

This project involves rock physics modeling of the Haynesville based on mineral and fluid densities and elastic stiffnesses. This is accomplished by applying effective medium modeling to densely sampled sonic and density logs from the borehole to interpret low frequency seismic data through the inversion of seismic data for p-impedance (Ip), S-impedance (Is), and density (rho) inversion, and grid-search-based rock physics inversion of these Ip, Is, and rho volumes. The basic theory in all of these topics is discussed here in chapter 3.

3.1 Background and Fundamentals

3.1.1 Anisotropy and the Stiffness Tensor

Hooke's law for linear elastic solids states that stress is proportional to strain and is expressed by the tensor relation:

$$\sigma_{ij} = C_{ijkl}\varepsilon_{kl}\ , \tag{3.1}$$

where σ_{ij} is the second rank stress tensor, ε_{kl} is the second rank strain tensor, and C_{ijkl} is the rank 4 stiffness tensor. Auld (1973) shows that based on symmetry and geometric considerations the stiffness tensor can be simplified to a 6 by 6 matrix (equation 3.2) with 21 independent elastic constants using Voigt notation.

$$\begin{bmatrix} \sigma_1 \\ \sigma_2 \\ \sigma_3 \\ \sigma_4 \\ \sigma_5 \\ \sigma_6 \end{bmatrix} = \begin{bmatrix} C_{11} & C_{12} & C_{13} & C_{14} & C_{15} & C_{16} \\ C_{12} & C_{22} & C_{23} & C_{24} & C_{25} & C_{26} \\ C_{13} & C_{23} & C_{33} & C_{34} & C_{35} & C_{36} \\ C_{14} & C_{24} & C_{34} & C_{44} & C_{45} & C_{46} \\ C_{15} & C_{25} & C_{35} & C_{45} & C_{55} & C_{56} \\ C_{16} & C_{26} & C_{36} & C_{46} & C_{56} & C_{66} \end{bmatrix} \begin{bmatrix} \varepsilon_1 \\ \varepsilon_2 \\ \varepsilon_3 \\ \varepsilon_4 \\ \varepsilon_5 \\ \varepsilon_6 \end{bmatrix} \tag{3.2}$$

This matrix can be simplified further for different symmetry conditions.

The simplest symmetry condition is present when a material is completely isotropic. Isotropy describes a material whose elastic properties are the same regardless of direction of propagation or polarization of the wave traveling through it. In the case of an isotropic medium, the stiffness tensor, C_{ij}, can be simplified to

$$C_{ij} = \begin{bmatrix} C_{11} & C_{12} & C_{12} & 0 & 0 & 0 \\ C_{12} & C_{11} & C_{12} & 0 & 0 & 0 \\ C_{12} & C_{12} & C_{11} & 0 & 0 & 0 \\ 0 & 0 & 0 & C_{44} & 0 & 0 \\ 0 & 0 & 0 & 0 & C_{44} & 0 \\ 0 & 0 & 0 & 0 & 0 & C_{44} \end{bmatrix} \tag{3.3}$$

where $C_{12} = C_{11} - 2C_{44}$, so that C_{ij} only has 2 independent elements.

However, most materials are anisotropic. The term anisotropy is used to describe a material whose properties are directionally dependent based on the direction of wave propagation and/or polarization (Tatham et al., 1992). Hexagonal anisotropy or transverse isotropy is an idealized anisotropic case in which a medium is isotropic in every direction perpendicular to an axis of symmetry. Transverse isotropy is commonly used as an approximation for the elastic condition of sedimentary rocks because it can be used to represent multiple adjacent isotropic layers that together are anisotropic. Vertical transverse isotropy (VTI) is the case in which this axis of symmetry is vertical, perhaps due to horizontal bedding and/or aligned clay minerals (figure 3.1). Horizontal transverse isotropy (HTI) is the case in which the axis of symmetry is horizontal, perhaps due to vertical fracturing (Tatham and McCormack, 1991).

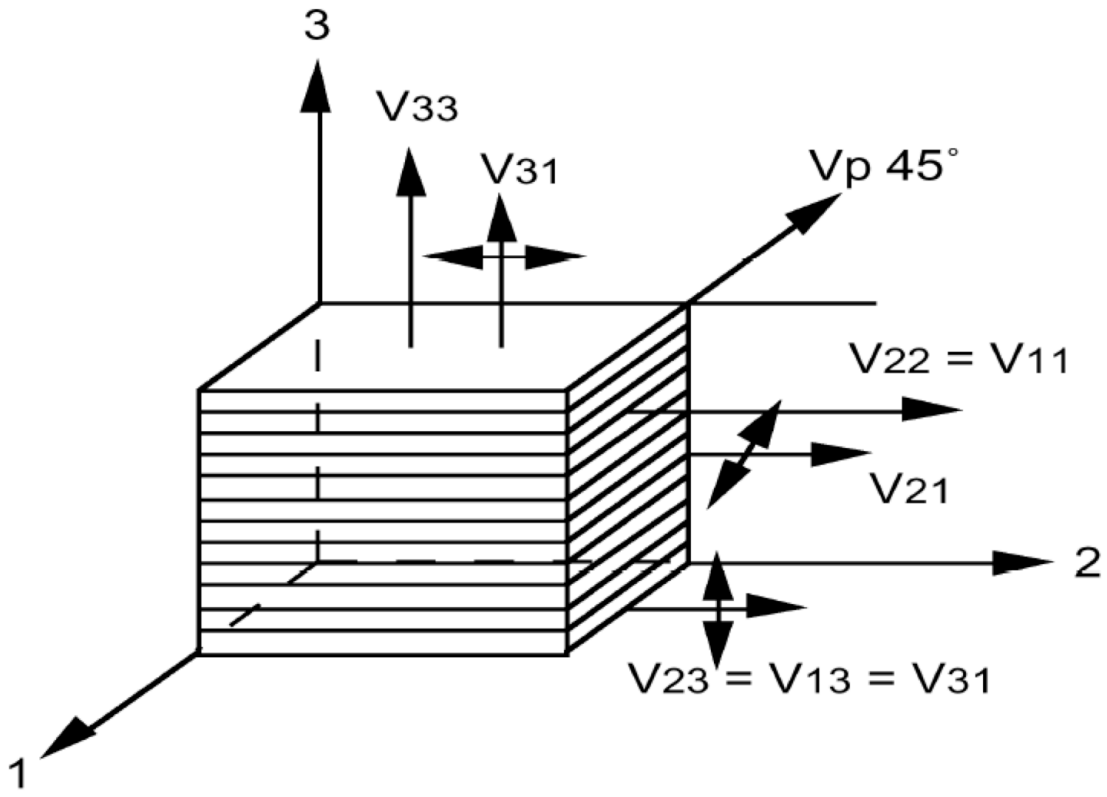

Figure 3.1: Schematic illustration of vertical transverse isotropy. Vertical transverse isotropy (VTI) has a faster horizontally propagating P-wave velocity than vertically propagating P-wave velocity and faster horizontally polarized horizontally traveling S wave (V_{21}) than horizontally polarized vertically traveling S wave (V_{31}). (Reproduced from course notes with permission from Kyle Spikes)

In this study, the Haynesville Shale, due to its horizontal layering, aligned clay flocculates and aligned high aspect ratio pores, is approximated as a VTI medium. The stiffness tensor for a VTI medium can be written as the following matrix (Rüger, 2002):

$$C_{ij}(VTI) = \begin{bmatrix} C_{11} & C_{12} & C_{13} & 0 & 0 & 0 \\ C_{12} & C_{22} & C_{23} & 0 & 0 & 0 \\ C_{13} & C_{23} & C_{33} & 0 & 0 & 0 \\ 0 & 0 & 0 & C_{44} & 0 & 0 \\ 0 & 0 & 0 & 0 & C_{44} & 0 \\ 0 & 0 & 0 & 0 & 0 & C_{66} \end{bmatrix} \tag{3.4}$$

where $C_{66} = \frac{1}{2}(C_{11} - C_{12})$, $C_{13} = C_{23}$, and where the axis of symmetry is in the vertical direction. In this case, C_{ij} has 5 independent elements. In formations with this symmetry, approximate C_{33} and C_{44} values can be calculated from vertical p-wave and s-wave velocities and density.

$$V_{33} = \sqrt{\frac{C_{33}}{\rho}} \tag{3.5}$$

$$V_{13} = V_{31} = V_{23} = V_{32} = \sqrt{\frac{C_{44}}{\rho}} \tag{3.6}$$

The horizontally traveling P- and S-wave velocities can be calculated by:

$$V_{11} = V_{22} = \sqrt{\frac{C_{11}}{\rho}} \tag{3.7}$$

$$V_{12} = V_{21} = \sqrt{\frac{C_{66}}{\rho}} \tag{3.8}$$

Anisotropy in these velocities are conveniently described by Thomsen's (1986) transverse anisotropy approximations:

$$\varepsilon = \frac{C_{11} - C_{33}}{C_{33}} \tag{3.9}$$

$$\delta = \frac{(C_{13} + C_{55})^2 - (C_{13} - C_{55})^2}{2C_{33}(C_{33} - C_{55})} \tag{3.10}$$

$$\gamma = \frac{C_{66} - C_{44}}{2C_{44}} \tag{3.11}$$

The low-frequency Stoneley wave velocity is approximately equal to V_{12}. By determining C_{66} from the Stoneley wave, γ can be estimated. ε can in turn be estimated from γ, such that C_{11} can be calculated. However, neither core measurements nor Stoneley wave information is available for this study. However, we can use well log measurements of vertical P- and S-wave velocities to describe 2 out of 5 elastic constants for a VTI medium (Mavko et al. 2009).

3.1.3 Frequency Dependence and Scales of Measurement

In reality, the stress-strain relationship is nonlinear and real rocks are inelastic. Thus, stiffness measurements (calculated from velocity from seismic or well log, or measured through deformation experiments in the lab) are dispersive, or frequency-dependent. This characteristic and the heterogeneity of rocks make the scale of measurement important. Seismic frequencies on the order of 5 to 120 Hz samples a much larger volume of rock with one wavelength than do sonic logs whose frequencies are on the kHz scale. This needs to be taken into account in this work as the modeling is done at the grain scale to represent well log-measured stiffness in order to model seismic scale (lower frequency) data. Upscaling well log scale models to understand how elastic properties and estimated rock properties appear at the seismic scale can be accomplished by using a moving Backus average. The moving Backus (1962) average simulates frequency-scaled data by harmonic averaging over a larger window, just as a passing wave samples over its entire wavelength as it passes through a medium (Backus, 1962). This technique is used in chapter 5 to compare 1D inversion results at well to results from applying the model to the seismic data.

3.2 Anisotropic Differential Effective Medium Model

3.2.1 Formulation and Physical Meaning

Effective medium models approximate a heterogeneous rock as an effective solid composed of idealized components. The overall elastic properties of the effective medium are calculated from the elastic properties of its components. In this work an inclusion-based effective medium model is used, the anisotropic differential effective medium (DEM) model. Figure 3.2 illustrates schematically the anisotropic DEM model. The square in 3.2a represents the mineral phase chosen as the initial background or 'host' material into which the yellow ellipsoids, representative of phase 2 mineral inclusions, will be added. Each inclusion aspect ratio is chosen from a normal distribution. Figure 3.2b depicts the process by which inclusions are added in a sequence of infinitesimal volumes. With the addition of each increment of phase 2, the effective elastic stiffnesses are calculated for that step. Those effective stiffnesses then represent the host medium for the addition of the next increments. This process is continued until the desired volume of phase two is added to phase one, and a final effective medium (3.2c) is reached. The change in stiffness dC^{DEM} due to the addition of the ith inclusion, of volume dv_i is:

$$dC^{DEM}(v) = \frac{dv_i}{1-v_i}(C^i - C^{DEM}(v))Q_i \tag{3.12}$$

where C^i is this stiffness of phase 2 , and Q_i is a geometric factor indicating ellipsoid shape and orientation relative to effective medium.

$$Q_i = [I + G_i(C_{DEM})(C_i - C_{DEM})]^{-1} \tag{3.13}$$

where I is the identity tensor, and G_i is a fourth rank tensor calculated from the response of the effective medium containing inclusion i (Eshelby, 1957; Mura, 1982).

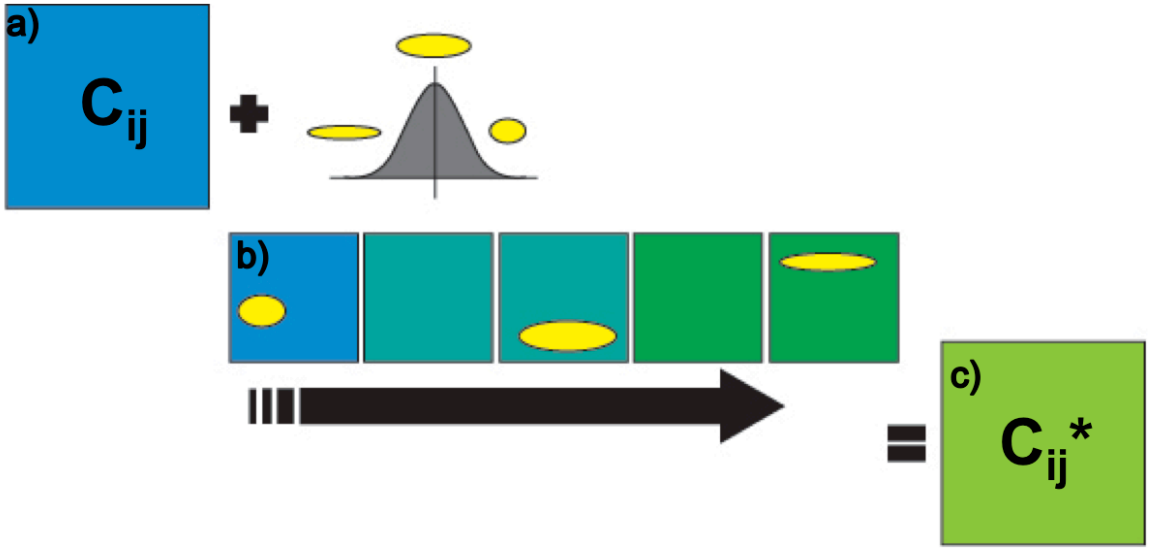

Figure 3.2: Anisotropic Differential Effective Medium (DEM) Model. a) The square represents the mineral phase chosen as the initial background or 'host' material into which the yellow ellipsoids, representative of phase 2 mineral inclusions (the aspect ratio of which is drawn from pdf), will be added. b) The five squares depict the process by which inclusions are added in infinitesimal volumes. With the addition of each increment of phase 2, the effective elastic stiffness tensor is calculated for that step. The result of each step then becomes the background medium for the following step. c) The final square represents the final effective medium after the desired volume of phase 2 is added.

The anisotropic DEM can be used iteratively to combine several different mineral and fluid phases. The order in which mineral phases are added is not trivial. In each step the 'host' material is treated as a framework material; framework minerals are connected at any volumetric proportion. Because of this, the order that mineral inclusions are incorporated creates a non-unique pathway. This order does not represent the natural

evolution of the rock, but instead the hierarchy of how rock components contribute to the overall stiffness of the material (Bandyopadhyay, 2009).

The formulation of the anisotropic DEM used here assumes a medium with VTI symmetry. All inclusions are aligned with their long axes perpendicular to a vertical axis of symmetry. As discussed above and in chapter 2, this assumption is appropriate for the Haynesville shale because of its aligned clay grains, clay-related pores, horizontal bedding, and scarcity of open vertical fractures.

3.2.2 Statistical Approach for Inclusion Shapes

In this modeling technique, I consider a distribution of inclusion shapes for each grain or pore type around a mean aspect ratio. This approach accounts for variation in grain and pore shapes. For each inclusion added, its aspect ratio is drawn from a normal probability distribution function (PDF) of aspect ratios appropriate for that inclusion. In addition, five different mean pore aspect ratios (and corresponding distributions) were considered as part of the model calibration (discussed in chapter 4). Including this statistical approach to inclusion shape helps to account for error in the simplification of grains and pores as idealized ellipsoids by allowing a range of shapes to impact the overall stiffness.

3.3 Rock Typing

Rock typing is the division of a particular formation into classes with similar elastic properties. These rock types can be modeled independently as separate rock fabrics. Figure 3.3 is a schematic illustration of how rock typing might be useful for improving estimation of velocities and elastic properties relative to a single model. Figure 3.3a shows an idealized rock composed of three types of grains with different grain

shapes. Figure 3.3b shows that by dividing the rock into three different rock types with different average mineralogies, each effective medium more closely resembles the rock properties of that interval. Figure 3.3c depicts the same section modeled with a single effective medium model. In this case, the resulting effective medium is less sensitive to changes in concentration of different minerals and is instead an average over the entire bulk rock volume. In this schematic example, mineralogy is the only parameter that is changed from one rock type to the other. This is for illustrative purposes only. Rock typing can be used to constrain any of the input parameters in a particular interval.

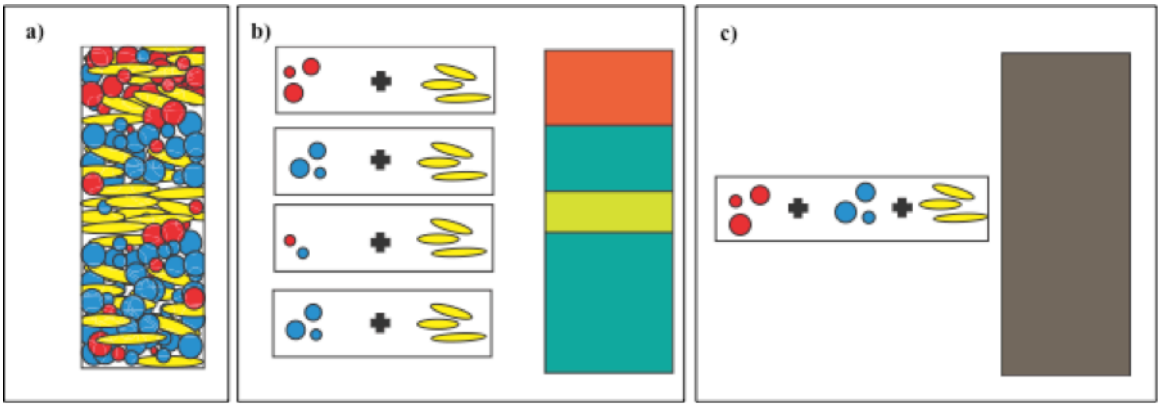

Figure 3.3: Rock Typing. a) An idealized rock composed of three types of grains b) Dividing the rock into three different rock types with different average mineralogy, each effective medium more closely resembles the rock properties of that interval. c) The same section modeled with a single effective medium model. In this case, the resulting effective medium is less sensitive to changes in concentration of different minerals, and is instead an average over the entire rock volume.

In the rock physics modeling portion of this thesis, the Haynesville is divided into two rock types based on the volumes of quartz, clay, and calcite content at each sampling point in depth. This is discussed in greater detail in chapter 4.

3.4 FLUID PROPERTIES

Fluid can properties significantly influence the seismic response of a rock. Considering realistic in-situ conditions and pore fluid composition is important for appropriately modeling this seismic response. It is especially important to quantify how much gas is likely to be in solution, because this can substantially lower moduli and viscosity of the fluid (Batzle and Wang, 1992). Batzle and Wang's (1992) empirically derived relations provide a means for estimating quantity of dissolved gas as well as the moduli, density, and viscosity of combined fluids based on the salinity, pressure, and temperature. Based on temperature and pressure gradients in the region the Haynesville Shale in the area of interest is about 69.5 Mpa and 112.89 degrees Celsius. Salinity estimates in the area in the literature range from about 50,000 ppm to 150 ppm. I assumed a salinity of 75,000 ppm. At any salinity above about 60,000 ppm, at these PT conditions, the amount of dissolved gas, according to the Batzle and Wang equations, becomes negligible. I, therefore, assume that there is zero dissolved gas.

Even without dissolved gas, the pore scale distribution of fluids and the saturation effect the seismic response. The two end members of fluid mixing conditions are "patchy" saturation, in which fluids are mixed at a very coarse scale (essentially isolated from each other in any given pore or group of pores), and uniform saturation in which fluids are mixed uniformly at a fine scale. These two scenarios can be represented, respectively, by the Voigt (arithmetic) and Reuss (harmonic) averages. The Voigt-Reuss-Hill is often taken as an estimate of the actual value by averaging these two upper and lower bounds (Mavko et al., 2009). The Haynesville Shale contains only brine and gas with an average brine saturation (from ECS logs) of about 0.42. The Batzle and Wang equations were used to calculate density and moduli of brine and gas independently at

Haynesville pressure and temperature. The Voigt-Reuss-Hill average was used to find the properties of the mixed fluid with a water saturation of 0.42. The resulting pore fluid properties used in this work are a density of 0.6 g/cm^3 (Table 3.1).

	Density (g/cm)	Bulk Modulus (GPa)	Shear Modulus (GPa)
Pore fluid	0.6	1.47	0

Table 3.1: Moduli and density of the pore fluid.

3.5 GRID SEARCHING

After the rock physics models were built, a technique called grid searching was used to estimate rock properties from the seismic data. Sen and Stoffa (1995) provide the grid searching technique for optimizing an inversion from large model space. Jiang (2014) demonstrates use of this grid-search technique for comparing P- and S-impedances from the rock physics models with those inverted from the seismic data and choosing the models that fall within accepted range of inverted value. In this work, I also filter the models based on density. The objective functions below constrain which models are accepted for each value from each trace.

$$Obj_P = \left| I_{P\mathrm{mod}el} - I_{Pinverted} \right| \le B_P \tag{3.14}$$

$$Obj_S = \left| I_{S\mathrm{mod}el} - I_{Sinverted} \right| \le B_S \tag{3.15}$$

$$Obj_\rho = \left| \rho_{\mathrm{mod}el} - \rho_{inverted} \right| \le B_\rho \tag{3.16}$$

B_p, B_s, and B_ϱ are the grid searching constraints on the difference between the model and the measurement for P-impedance, S-impedance, and density, respectively. Use of the objective functions provides multiple accepted values. The mean value and standard deviation were then calculated for each set of accepted models to provide a best estimate and corresponding uncertainty.

3.6 Model Based Impedance and Density Inversion

Many different inversion algorithms are available to estimate impedance and densities from seismic reflectivity. For this work, I generated near, mid, and far stacks from the Haynesville seismic (described in greater detail in chapter 5) and performed simultaneous model-based inversion to obtain P-impedance, S-impedance, and density. This inversion was performed using commercial Hampson-Russell© software using an algorithm with three assumptions: a linearized approximation for reflectivity, angle dependent reflectivity (Aki and Richards, 2002), and linear relationships among the logarithms of P-impedance, S-impedance, and density (Hampson et al., 2005).

3.6 References

Aki, K., and P. G. Richards, 2002, Quantitative Seismology, 2nd Edition: W. H. Freeman and Company.

Auld, B.A., 1973, Acoustic fields and waves in solids, Vol. 1 and 2, John Wiley & Sons, Inc., New York.

Backus, G. E., 1962, Long wave elastic anisotropy produced by horizontal layering: Journal of Geophysical Research, **67**, 4427-4440.

Bandyopadhyay, K., 2009, Seismic anisotropy: geological causes and its implications to reservoir geophysics: Ph.D. thesis, Stanford University.

Batzle, M., and Z. Wang,1992, Seismic properties of pore fluids: Geophysics, **57**, No. 11, 1396-1408.

Eshelby, J. D., 1957, The determination of the elastic field of an ellipsoidal inclusion and related problems: Proceedings of the Royal Society of London, Series A, **241**, 376-396.

Hampson, D. P., B. H. Russell, and B. Bankhead, 2005, Simultaneous inversion of prestack seismic data: 75th Annual International Meetings, SEG, Expanded Abstracts, 1633–1636.

Jiang, M., 2014, Seismic Reservoir Characterization of the Haynesville Shale: rock-physics modeling, prestack seismic inversion and grid searching: PhD thesis, The University of Texas at Austin.

Mavko, G., T. Mukerji, and J. Dvorkin, 2009, The Rock Physics Handbook: Tools for Seismic Analysis of Porous Media: Cambridge, University Press.

Mura, T., 1982, Micromechanics of Defects in Solid: Martinus Nijhoff Pub.

Rüger, A., 2002, Reflection coefficients and azimuthal AVO analysis in anisotropic media: Society of Exploration GeophysicsMonograph Series.

Sen, M. and P. L. Stoffa, 1995, Global optimization methods in geophysical inversion: ELSEVIER Science.

Tatham, R.H. and McCormack, M.D., 1991, Multicomponent seismology in petroleum exploration: Investigation in Geophysics Series, **6,** Society of Exploration Geophysicists.

Tatham, R.H., Matthews, M.D., Sekharan, K.K., Wade, C.J., and Liro, L.M., 1992, A physical model study of shear-wave splitting and fracture intensity: Geophysics, **57**, No. 20, p. 647-652.

Thomsen, L., 1986, Weak elastic anisotropy: Geophysics, **51**, 1954–1966, doi: 10.1190/1.1442051.

Chapter 4: Rock-type model characterization of the relationship between elastic and reservoir properties in the Haynesville Shale

4.1 INTRODUCTION

The best recovery of hydrocarbons from unconventional reservoirs occurs in zones optimal for horizontal drilling and hydraulic fracturing and in locations with high gas concentration. Characterization of the relationship between important rock properties, such as mineralogy, rock fabric, and fluid saturation with elastic properties of the Haynesville shale will improve our ability to identify these optimal locations from seismic and well log data. In this work, the elastic properties of the Haynesville are modeled using the anisotropic DEM model, which allows for parameterization of pore and grain aspect ratios, mineral composition, and load bearing matrix. We divided the Haynesville into two separate rock types: a calcite-rich rock type and a clay- and silica-rich rock type. Rock typing provided for greater sensitivity of the rock type models to mineral content, which provided an improved porosity versus stiffness and combined porosity plus kerogen versus stiffness trend for the calcite-rich rock type.

In this chapter, the anisotropic DEM represents the complex mineralogy of the Haynesville by building the rock matrix with iterative additions of five mineral phases and fluid-filled porosity. The anisotropic DEM incorporates the effects that pore and grain shapes have on rock stiffness and anisotropy due to their depositional alignment. This representation is done with a statistical formulation of the anisotropic DEM that incorporates a distribution of grain and mineral shapes around a mean aspect ratio. To reduce the parameter space of the models, two separate rock types based on composition are modeled independently using the anisotropic DEM.

4.2 ROCK TYPING

As discussed in chapter 3, rock typing is the division of a particular interval into classes with distinct rock properties. These rock types can be modeled independently of each other to represent the porosity-stiffness trend of each type. Rock typing can be used to model distinct lithologies; however, we use it to separate lithofacies with different mineral compositions within the Haynesville. As a result, effective medium models are more sensitive to small changes in mineralogy. This sensitivity is important when the models are being used in seismic inversion scenarios to evaluate brittleness and propensity for fracturing.

I divided the Haynesville Shale into two unique rock types based on a statistical clustering algorithm, K-means, that minimized the sum of distances within a cluster to the centroid of the cluster (Spath, 1985). Two rock types resulted based on quartz, calcite, and clay volumes. These rock types are rock type (1), which is calcite rich, and rock type (2), which is calcite-poor, but clay and silica rich. The location of these rock types with depth is shown in figure 4.1 alongside the ECS log of the key minerals.

Rock type 1 occurs predominantly in the shallowest portion of the Haynesville Shale, whereas rock type 2 occurs predominantly in the deeper portion of the Haynesville. The ECS logs show that the quartz and clay volumes track each other well within the Haynesville. With a change from rock type 2 to rock type 1, an increase in calcite and a decrease in clay and silica occurs, but the ratio between the two siliciclastics is approximately one throughout the shale.

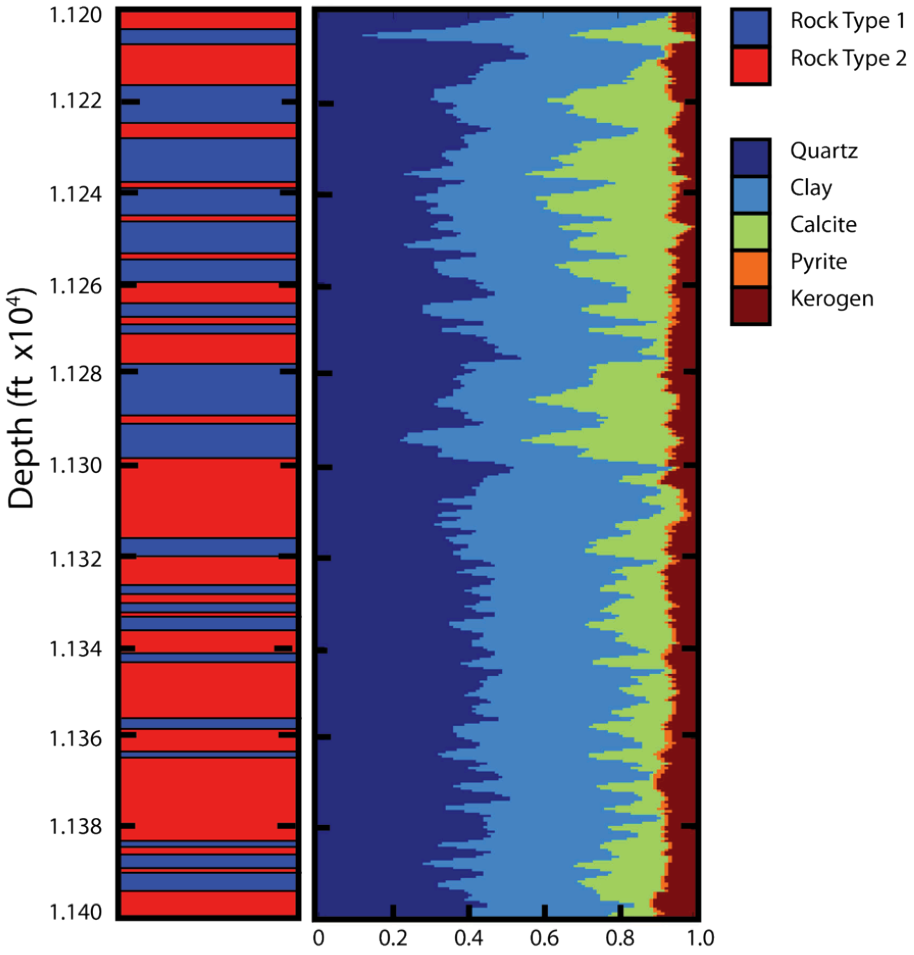

Figure 4.1: (Left) The locations of calcite-rich rock type 1 (blue) and the quartz- and clay-rich rock type 2 (red) versus depth. (Right) Corresponding ECS mineral logs plotted versus depth.

4.4 CALIBRATION

Before computing models with idealized mineralogy and porosity, the model was first calibrated by using ECS mineralogy and porosity calculated from well logs as inputs, such that each modeled point represents measured composition and porosity pair. This initial calibration of the model provided the order of phases and ensured that using only

five mineral phases was adequate to predict elastic properties. Using measured mineral compositions with associated porosities ensured that the only free parameters in the calibration were the order of phase input and aspect ratio of grains and pores.

In our model, we simplified the mineralogy of the Haynesville to 5 mineral phases: clay, quartz, calcite, kerogen, and pyrite. The densities and moduli of the pore and solid inclusions used in the modeling are listed in Table 4.1. All mineral phases were treated as isotropic inclusions with varying aspect ratios. Their densities take into account that each modeled mineral phase incorporates multiple minerals as discussed in chapter 2 and illustrated in table 2.1 and figure 2.5. These adjusted densities are listed below along with the fluid properties calculated in chapter 3.

Mineral Phase	Density (g/cm)	Bulk Modulus (GPa)	Shear Modulus (GPa)
Quartz	2.65	37	44
Calcite	2.71	76.8	32
Clay	2.6	21	7
Pyrite	4.93	147.4	132.5
Kerogen	1.3	2.9	2.7
Fluid-filled Pore	0.6	1.47	0

Table 4.1: Moduli and densities of the solids and fluid-filled pores

We assumed aspect ratios of 1 for quartz and calcite. This is appropriate because these minerals are very stiff, and grain shape changes have negligible effects. The aspect ratios for soft phases, clay and kerogen, were chosen as 0.1 and 0.01, respectively. Calcite, quartz, and clay were each respectively tested as the framework mineral. In each case, the mineral selected as a host served as a solid homogenous matrix and did not require an aspect ratio input. This calibration was performed on each rock type separately

to test for sensitivity of the model to small changes in rock fabric. For both rock-types calcite provided the best results as the framework mineral.

In addition to calibrating the phase input order, five different mean pore aspect ratios were tested 0.5, 0.3, 0.2, 0.1, and 0.05 for each rock type. Every pore in each calibrated point was drawn from a distribution around each of those mean pore aspect ratios. The results of the calibrations are plotted in figures 4.2 and 4.3. In each figure, a and b show well A C_{33} and C_{44} values, respectively, plotted against the modeled values at those porosity and mineralogy inputs. The data points are colored by pore aspect ratio input to the model. The black line represents a one to one ratio between modeled and measured. In c and d, the modeled data points are plotted against input porosity. Black points represent actual C_{33} and C_{44} values.

For rock type 1 the mean pore aspect ratio of 0.3 provided the best fit. For rock type 2, none of the pore aspect ratios predicted well C_{33} and C_{44} as a function of porosity in the calibration. Figures 4.3c and 4.3d illustrate that in rock type 2, there seems to be little change of the Cij values with increased porosity. However, a pore aspect ratio of 0.3 still better predicted the Cijs than any of the other pore aspect ratios. This calibrated pore aspect ratio is used in further modeling.

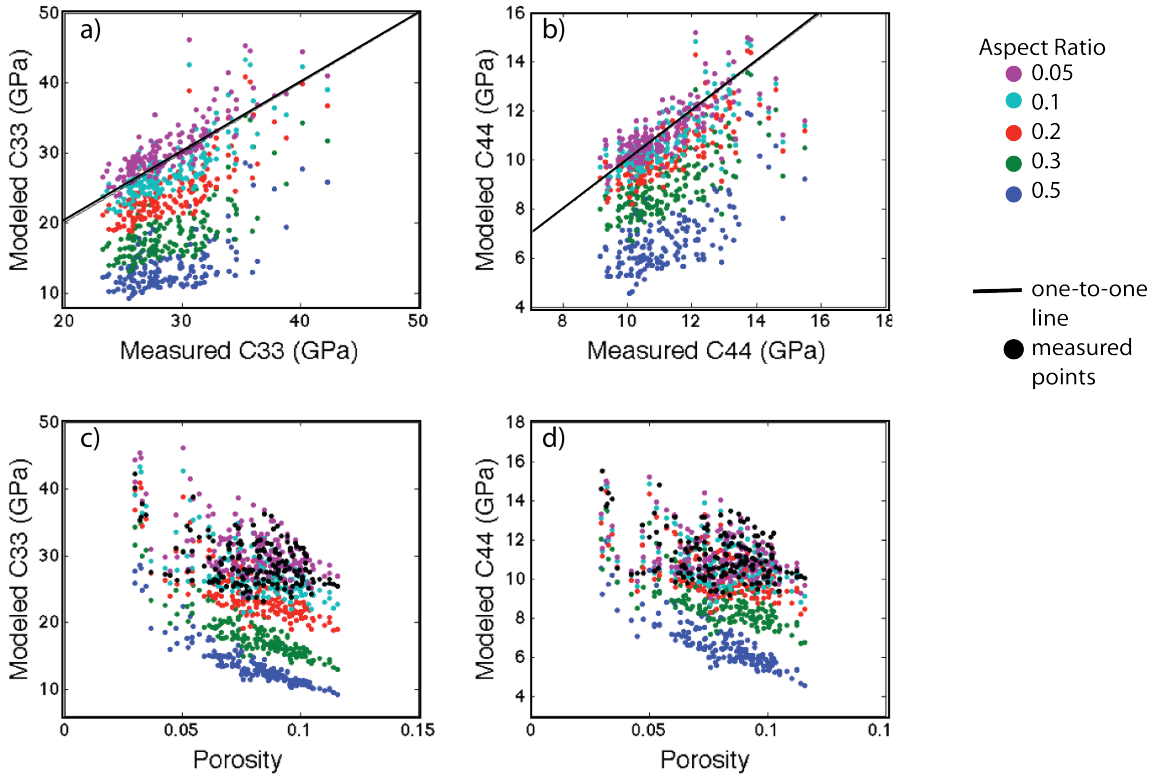

Figure 4.2: Calibration of Rock Type 1. Calcite was used as host material. Phases 2, 3, 4, and 5 were, respectively, quartz, clay, pyrite, and kerogen. Porosity was added last as phase 6. a) and b) show well A C_{33} and C_{44} values, respectively, plotted against the modeled values at those porosity and mineralogy inputs. c) and d) show the relationship between modeled C_{33} and C_{44} and porosity at the same range of pore aspect ratios, colored as in a) and b). Black circles represent measured $C_{33}$and C_{44} values. Colored points represent each of 5 pore aspect ratios : 0.5, 0.3, 0.2, 0.1, and 0.05.

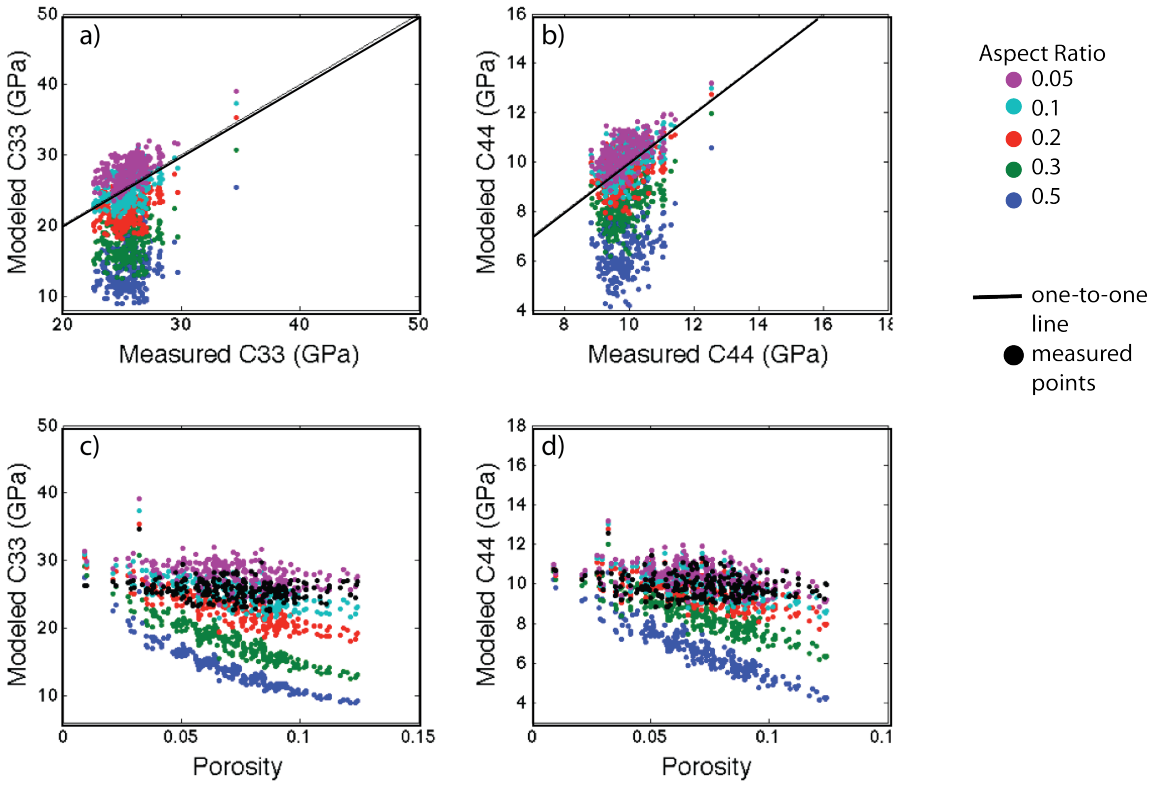

Figure 4.3: Calibration of Rock Type 2. Calcite was used as host material. Phases 2, 3, 4, and 5 were respectively quartz, clay, pyrite, and kerogen. Porosity was added last as phase 6. a) and b) show well A C_{33} and C_{44} values, respectively, plotted against the modeled values at those porosity and mineralogy inputs. c) and d) show the relationship between modeled $C_{33}$and C_{44} and porosity at the same range of pore aspect ratios, colored as in a) and b). Black circles represent measured $C_{33}$and C_{44} values. Colored points represent each of 5 pore aspect ratios: 0.5, 0.3, 0.2, 0.1, and 0.05.

4.5 RESULTS

Using the mineral phase input order and the calibrated mean pore aspect ratio, I created six idealized model lines with decreasing calcite and with increasing clay, silica, and kerogen. The compositions associated with each model line are shown in Table 4.2. Silica and clay are increased simultaneously and equivalently as calcite is reduced. Kerogen is increased steadily from 2 to 11 percent as clay and silica are increased

because clay and kerogen volumes are correlated within the Haynesville Shale. Pyrite is held at a constant 2 percent. All six models are plotted together with measured C_{33} and C_{44} values in Figure 4.4 with rock type 1 (red) and rock type 2 (blue).

Line Color	Calcite	Quartz	Clay	Pyrite	Kerogen
1. Blue	54	21	21	2	2
2. Green	40	27	27	2	3
3. Red	31	31	31	2	5
4. Cyan	21	35	35	2	7
5. Magenta	10	40	40	2	8
6. Yellow	1	43	43	2	11

Table 4.2: Mineral assemblages of six idealized model lines

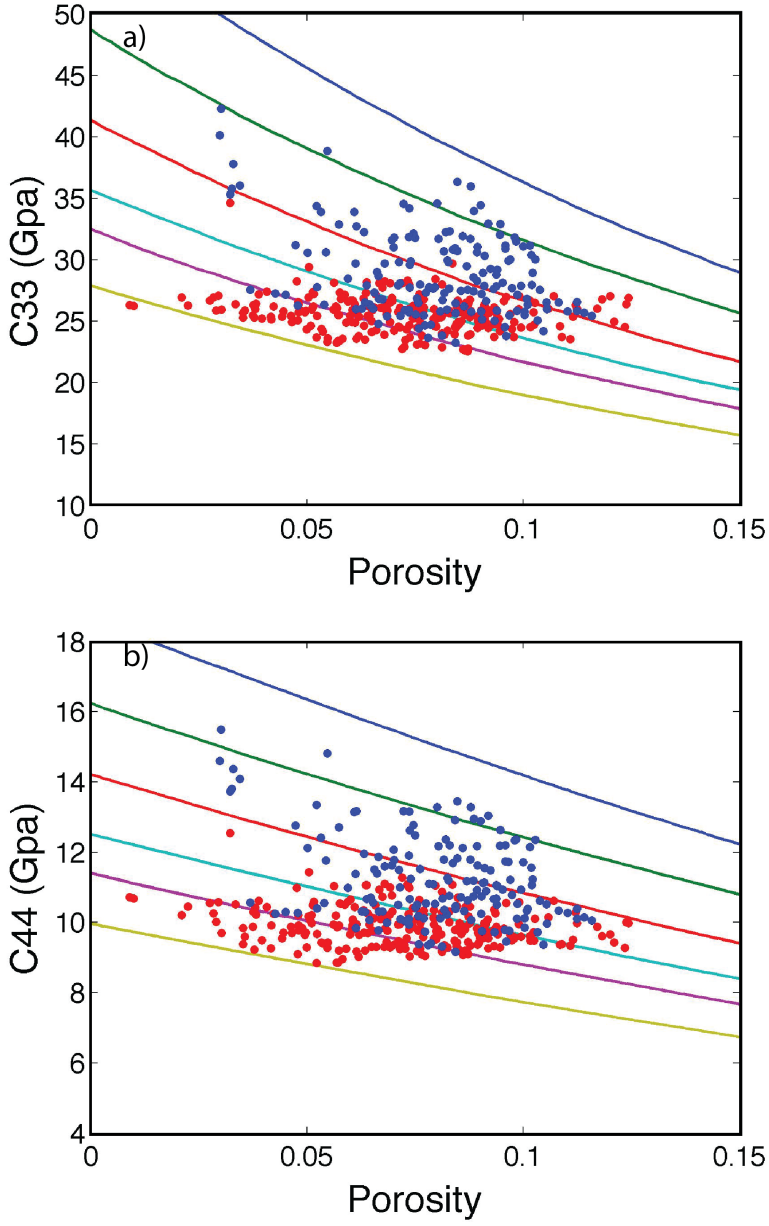

Figure 4.4: Porosity vs elastic stiffness components C_{33} (top) and C_{44} (bottom). Six model lines with distinct mineral assemblages (Table 4.2) are plotted with measured values of porosity and stiffness. Points that fall within rock type 1 are colored blue; rock type 2 points are shaded red.

Of the minerals used in the modeling, calcite has the highest bulk modulus with the exception of pyrite, which only occurs in very small quantities in the Haynesville. In the model lines, as calcite volume is reduced and quartz and clay volumes are increased, the C_{33} component is also reduced. Clay has a relatively low shear modulus, and the stiffness component C_{44} is reduced with reduction in calcite and increase in siliciclastics. As expected by mineral content in each type, rock type 1 is best characterized by the most calcite-rich model lines, whereas rock type 2 is better described by the clay and silica rich model lines.

Hydraulic fracture energy can be used most efficiently in brittle intervals with high elastic stiffness. Rock type 1, which occurs predominantly in the upper half of the Haynesville, has higher calcite content and larger elastic stiffness components C_{33} and C_{44}. To characterize further this interval of the Haynesville, we examine the stiffness trend of rock type 1 with respect to combined porosity and kerogen. Because of its low elastic moduli, kerogen affects the seismic velocity in manner similar to porosity. The same six model lines seen in Figure 4.4 are evaluated in Figure 4.5 but are shifted according to the kerogen content in each modeled mineral assemblage. The models describe the stiffness versus porosity plus kerogen trend in rock type 1 quite well. The measured points, colored by calcite, fall close to the appropriate mineral assemblage model lines. A cluster with low combined porosity and kerogen fall outside of model lines. These points have less than 2% kerogen, and they are outliers with respect to the overall stiffness versus porosity and kerogen trend.

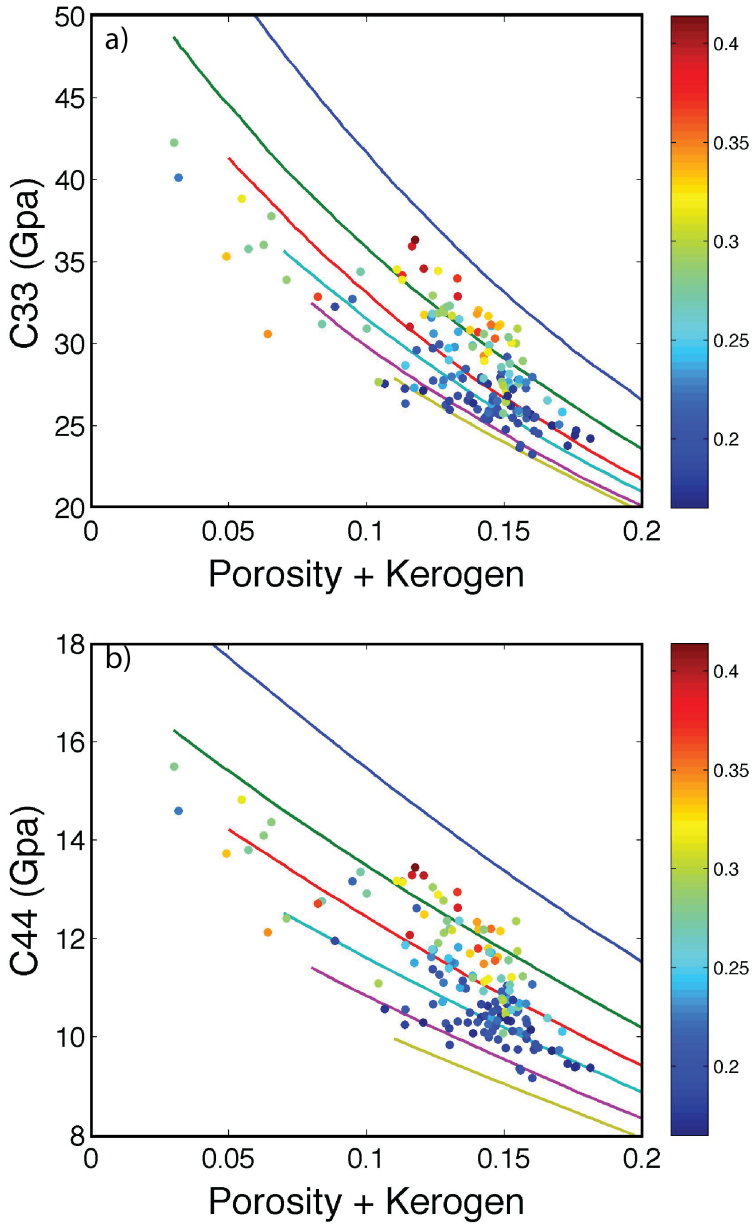

Figure 4.5: Porosity plus kerogen versus elastic stiffness components C_{33} (top) and C_{44} (bottom) of tock type 1. Six model lines with distinct mineral assemblages (Table 4.2) are plotted. The points are measured values of stiffness as a function of the sum of porosity and kerogen. The colorbar coresponds to calcite volume.

4.6 Discussion and Conclusions

Porosity, ECS mineral logs, the phase order and inclusion shapes, all inputs to the anisotropic DEM, characterize the composition and fabric of the Haynesville Shale. The ECS and XRD mineralogy data are measured independently of the sonic measurements used to calculate stiffness components. This prevents biasing of the model calibration and results.

In this work, calibration and modeling was performed on two statistically determined compositional rock types within the Haynesville Shale. Calcite-rich models better described calcite-rich rock type 1. Clay and quartz-rich rock type 2 was better described by models with reduced calcite content. Data from rock type 2 were not constrained as well by the model as was rock type 1. This situation could be a result of the larger uncertainty in elastic properties of the softer clay and kerogen phases, which are more abundant in this rock type. In addition, all clays and chlorite in clay matrix were considered a single phase in the modeling. Accounting for proportions of chlorite and illite within the clay in this rock type might improve the model.

Trends of stiffness versus porosity and stiffness versus the sum of porosity and kerogen within calcite-rich rock type 1 are well constrained by the 6 model lines that have distinct mineral assemblages. Measured stiffnesses fall close to model lines with appropriate calcite and kerogen composition. Poorer model matching occurs with increased clay and kerogen content which, like model mismatch in rock type 1, can be explained in terms of uncertainty in elastic properties of these softer phases. In proximity to this well (and as we saw previously in chapter 2 in proximity to well B too), the upper portion of the Haynesville contains a higher percentage of calcite rich rock type 1 and will yield more efficient use of hydraulic fracture energy. For characterization of the

spatial distribution of the calcite-rich and clastic rich intervals within the Haynesville Shale in 3D, this model is used for inverse calculation in the following chapter from Ip, Is, and density volumes inverted from 3D prestack seismic data .

4.7 REFERENCES

Spath, Helmuth. The cluster dissection and analysis theory fortran programs examples, Prentice-Hall, Inc., 1985.

Chapter 5: Application of rock-physics model, grid searching, and seismic inversion for characterization of porosity and mineralogy in the Haynesville Shale

This chapter combines both forward and inverse calculations to estimate the distributions of porosity and mineral concentrations for the Haynesville Shale. The forward modeling consists of computing a model space containing 10 iterations of 50 different mineral compositions over a given porosity range. The inverse calculation is done through a grid searching method (Sen and Stoffa, 1995; Jiang, 2014) that searches the model space to provide a best estimate of rock properties and corresponding uncertainty by providing a range of property estimations. This same technique is performed both in 1D on well A and in 3D on impedance and density volumes inverted from a 3D seismic volume.

5.1 1D Grid Searching and Rock Properties Inversion

The workflow is first applied to a 1D dataset, the Ip, Is, and density logs from well log A. These data were used to constrain grid searching from the model along with density.

5.1.1 Prior Distributions

As discussed in chapter 2, the mineral composition of the Haynesville is predominantly quartz, clay, and calcite with an increase in calcite corresponding to a decrease in siliciclastics. However, no strong correlation or anticorrelation exists between quartz and clay minerals (figure 2.6). Fifty prior composition assemblages were created to represent the anticorrelation of siliciclastics and carbonates while maintaining a ratio of one between quartz and clay phases. The percentages of calcite, quartz, kerogen, and clay were varied in each assemblage. A uniform prior distribution of porosity was applied

such that for each mineral composition assemblage, porosities from 0 to 25 percent were modeled. Pore aspect ratios for every modeled pore inclusion were drawn from a normal distribution around the mean pore aspect ratio of 0.3 (calibrated in chapter 4). Ten iterations were calculated of each porosity-mineral pair such that a different range of pore aspect ratios is used in each porosity-mineral model. These prior distributions for mineral assemblage, porosity, and pore aspect ratio are illustrated in figure 5.1.

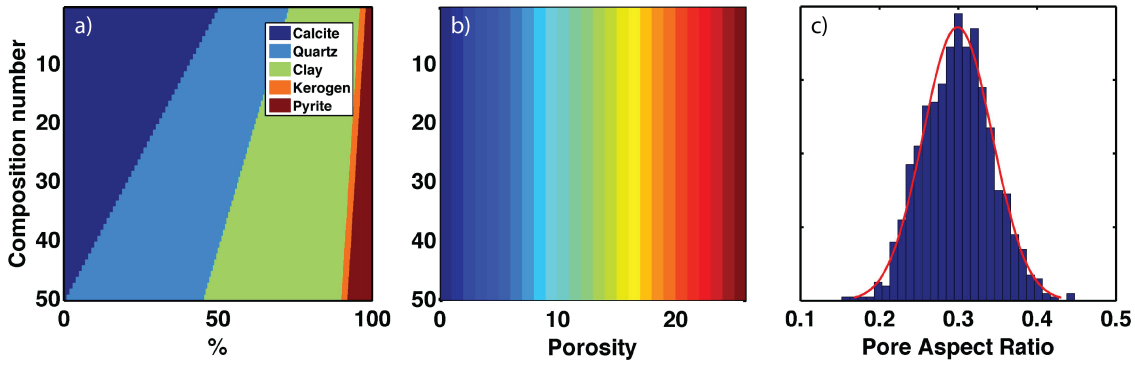

Figure 5.1: a) Represents the prior distribution of mineral compositions via 50 mineral assemblages: mineral percent on the x axis, composition number on the y axis. As calcite decreases, quartz and clay simultaneously increase. Kerogen also increases with a decrease in quartz; pyrite remains at 2 percent in every assemblage. b) The prior distribution of porosity is uniform with a model point represented at every 1 percent increase in porosity from 0 to 25 percent porosity. The porosity is on the x axis and the composition number is on the y axis. c) Represents what any distribution of pore aspect ratios may look like for a given model and set of porosity points. Each pore aspect ratio is drawn from a normal distribution around 0.3.

5.1.2 Modeling Space

The rock physics model designed and calibrated in chapter 4 is used in this 1D inversion and in the subsequent 3D inversion of seismic data. The modeling space of 12500 modeled points generated by the prior distributions of mineral composition,

porosity, and pore aspect ratio from the anisotropic DEM model are plotted in figure 5.2. Figures 5.2a and 5.2b show porosity plotted against elastic stiffness components C_{33} and C_{44}. Figure 5.3c and 5.3d show density plotted against Ip and Is, respectively, which are the three properties constraining the objective functions for the rock physics inversion.

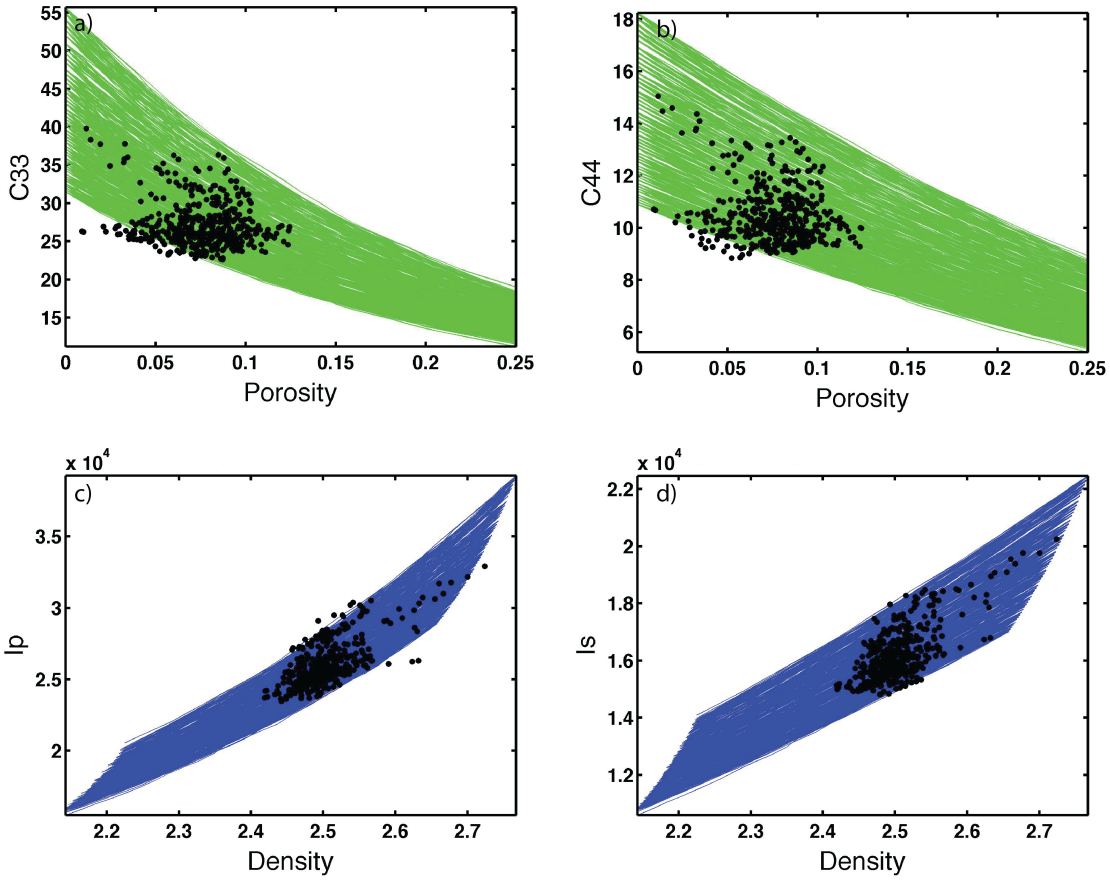

Figure 5.2: Models used in the inversion consisting of 10 iterations of 50 different mineral compositions over a given porosity range from 0 to 25 percent. a) and b) show porosity plotted against elastic stiffness components C_{33} and C_{44}. c) and d) show density plotted against Ip and Is respectively, which are the three properties constraining the objective functions for the rock physics inversion.

In both porosity-stiffness space and density-impedance space, there are data points that fall outside of the model space. They still fall within the bounds of the objective function and will still be assigned a model during the inversion. I do not, within any of the prior distribution model assemblages, provide a case with 0 value for any mineral. This is because the hierarchy in which the mineral phases are added changes the entire model trend line. I also constrain the rate at which there is a decrease in carbonate fraction corresponding to an increase in siliciclastics while holding quartz content equal to clay content. Measured values with zero kerogen or zero calcite fall accordingly above or below the model space. These points will be assigned very low values of these minerals in the inversion but will not be assigned values of zero.

5.1.3 Grid Searching & Objective Function

The grid searching technique used by Jiang (2014) compares P- and S-impedances from the rock physics models with those inverted from the seismic data and chooses the models that fall within the accepted ranges of the inverted values. This provides a range of models to account for uncertainty in inversion for impedance and density volumes and in rock property estimation. The objective functions described in chapter 3 are used here, but with the objective bounds, 300 (g/cc)*(ft/s) for both P- and S-impedances and 0.3 g/cc for density:

$$Obj_P = \left| I_{P\,\mathrm{model}} - I_{Pinverted} \right| \leq 300 \tag{5.1}$$

$$Obj_S = \left| I_{S\,\mathrm{model}} - I_{Sinverted} \right| \leq 300 \tag{5.2}$$

$$Obj_\rho = \left| \rho_{\mathrm{model}} - \rho_{inverted} \right| \leq .3\ . \tag{5.3}$$

5.1.4 1D Results and Discussion

Figure 5.3 shows the results of the grid searching for porosity colored by probability. The porosity with the highest probability is indicated by a black line and the measured values from the well log are indicated by a white line. The inversion predicted the overall porosity trend through much of the depth range. The root mean square (RMS) of the difference is 0.022. However, there are several isolated intervals in which the porosity is significantly overestimated or underestimated. Figure 5.4 contains the mean mineral composition from the grid searched models. From left to right the panels display calcite, quartz, clay, and kerogen. Pyrite is not displayed because it was held constant in all model iterations. The red line indicates the modeled mineral volume, and the black line indicates the ECS measured volume of that mineral. The modeled calcite percentages provide good estimates of the measured ECS logs at well A. The best fit calcite result follows the trend of the measured calcite very well and predicts many of the peaks and troughs. The root mean square (RMS) of the difference between the measured and the modeled calcite is 7.2 percent. However, we see that the same regions with large errors in the porosity estimation have corresponding noticeable errors in calcite volume. The clay and quartz inversion results are identical because all models had a quartz-clay ratio of one. The RMS of the difference between the measured and modeled values of both quartz and clay is 5.9 percent. However, the results do not predict large changes in either mineral well. Modeled kerogen estimates the measured kerogen trend throughout most of the depth, but it slightly under predicts kerogen at the base of the well. The RMS difference in kerogen is 1.9 percent.

The regions that showed the largest error in all inversion results are regions with anomalously high or low clay to quartz ratios. Other prior distributions of quartz to clay

ratio were investigated, including a normal distribution in the ratio of clay to quartz and distributions that favored higher percentages of each quartz and clay. These distributions were evaluated to provide a modeling space that describes intervals that were not predicted well by the models investigated here. This change in the prior distribution did in some cases improve the match between the modeled siliciclastic minerals and measured in those regions, but always to the detriment of the porosity, kerogen, and calcite prediction in all other intervals. Because a prior distribution considering a constant quartz-clay ratio of 0.5 predicted the calcite, kerogen, and total siliciclasic content, this distribution was used in the 3D inversion.

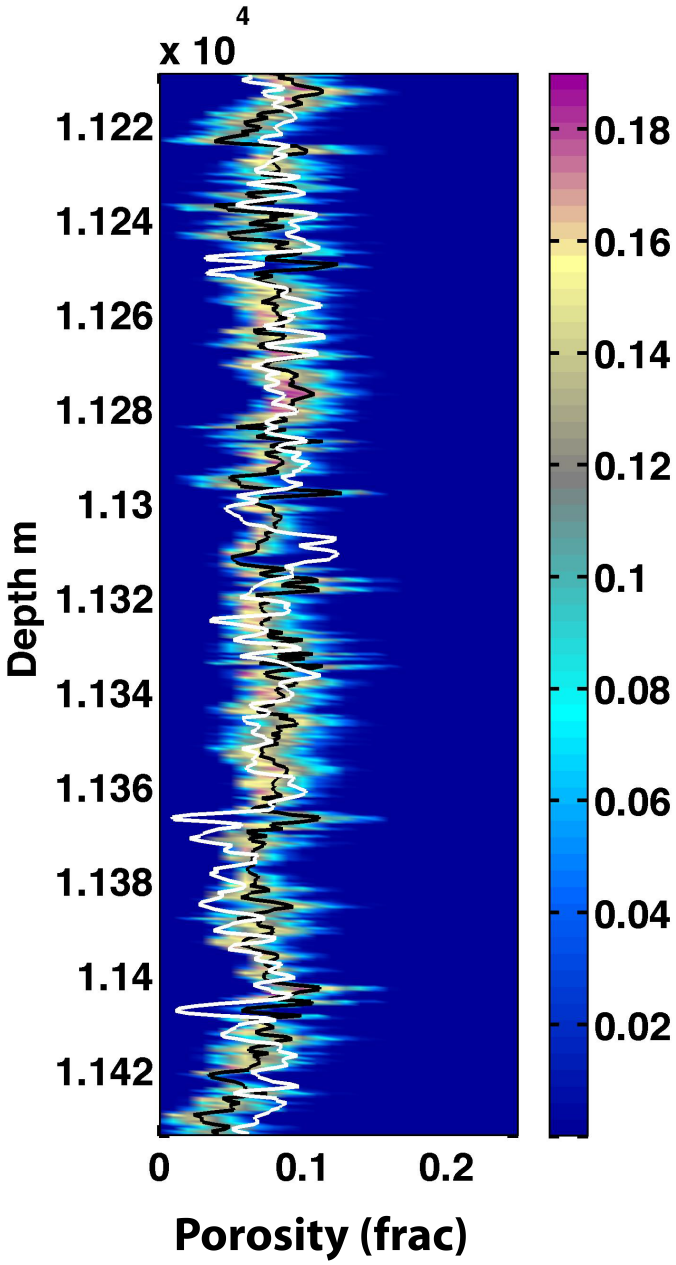

Figure 5.3: This plot shows porosity colored by probability based on the grid searched model points with depth. The porosity with the highest probability is indicated by a black line, while the measured values from the well log are indicated by a white line. The root mean square (RMS) of the absolute value of the difference between the most likely porosity and the measured is 0.022.

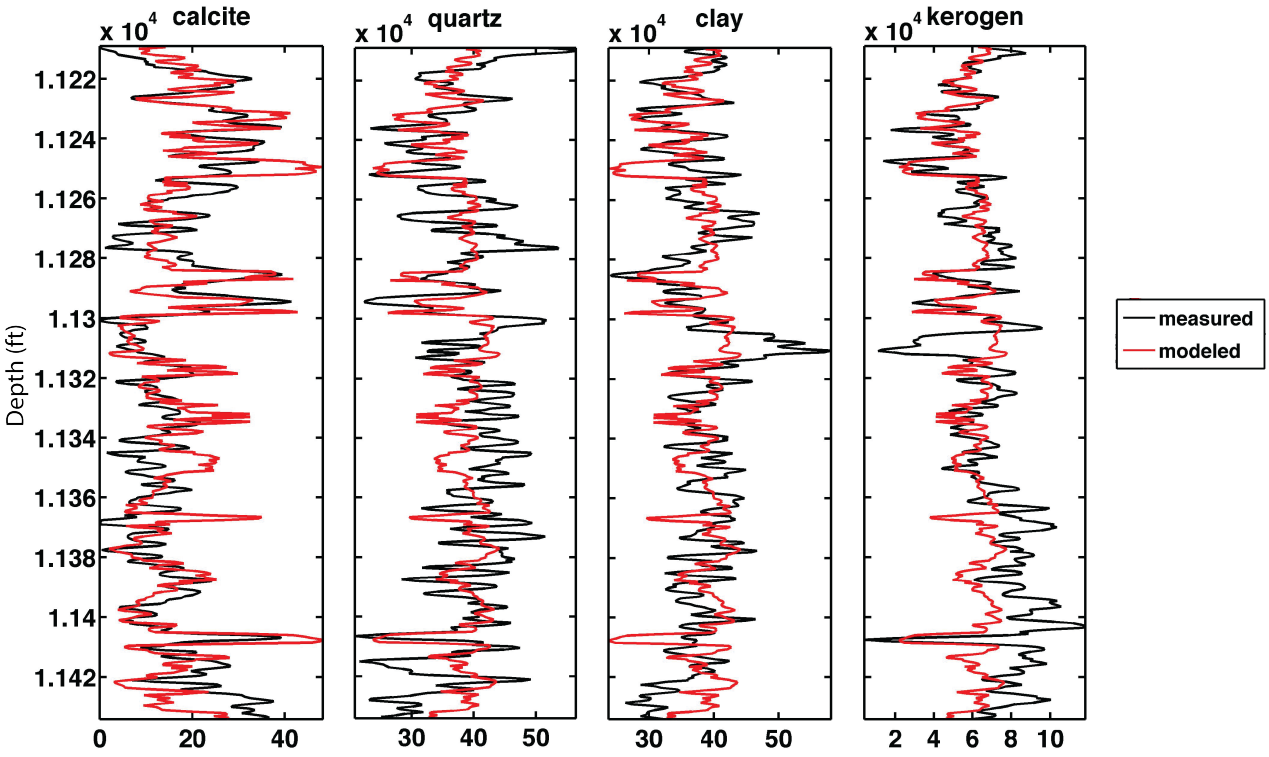

Figure 5.4: Display of 1D inversion results for (from left to right) calcite, quartz, clay, and kerogen. The black line indicates the ECS measured volume of that mineral, and the red line indicates the best match from the inversion.

5.2 3D Impedance and Density Inversion, Grid Searching, and Rock Properties Inversion

5.2.1 Simultaneous Inversion for Ip, Is, and Density

To generate Ip Is, and density volumes, I performed simultaneous model-based inversion. This inversion was performed using commercial Hampson-Russell© software using an algorithm with three assumptions: a linearized approximation for reflectivity, angle dependent reflectivity (Aki and Richards, 2002), and linear relationships among the logarithms of P-impedance, S-impedance, and density (Hampson et al., 2005).

An angle gather of 20 bins over 60 degrees from the prestack data was generated to determine which angles contain useful information about the interval of interest. This angle gather is depicted in figure 5.5 with the Haynesville highlighted in green and the P-wave log from well B superimposed in red. Well B was logged for the majority of the borehole length, and thus, is used in the well tie and as the training well for the model based inversion. Well A, which was logged only in the Haynesville interval, is the test well for the model-based inversion. At angles larger than about 48 degrees, reflectivity within the Haynesville appears relatively noisy. Seismic information contained only within incidence angles 2 through 48 were used in the inversion. A supergather of near, mid, and far stacks around the angles 10, 25, and 40 degrees was generated for use in the partial stack inversion (figure 5.6).

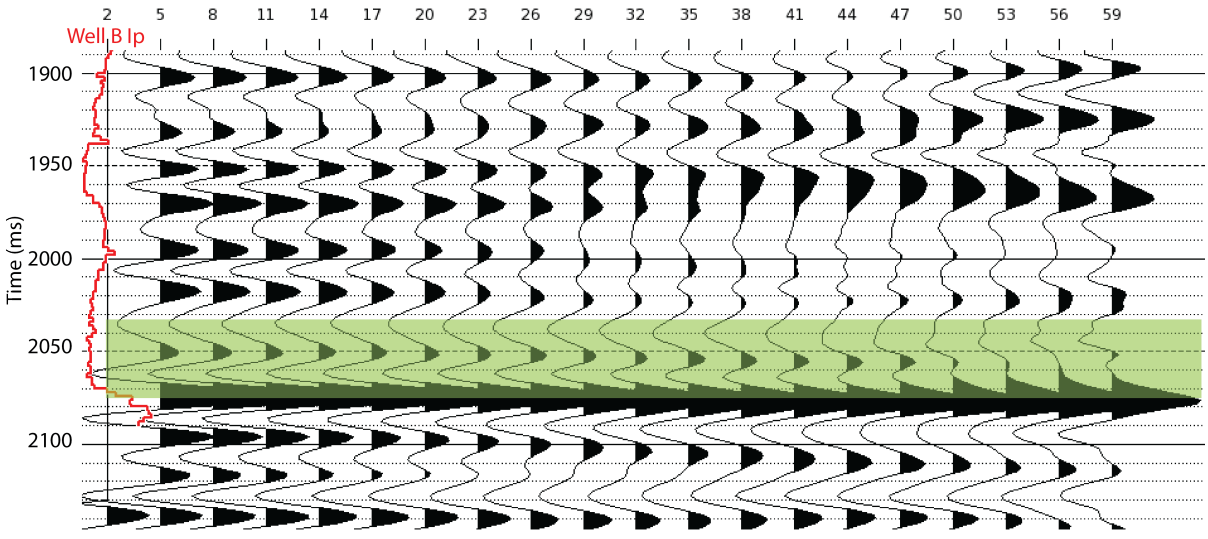

Figure 5.5: Angle gather from the prestack seismic at well B. The x-axis shows 20 angle bins over 60 degrees. The Haynesville is highlighted in green. The Ip log from well B is superimposed in red.

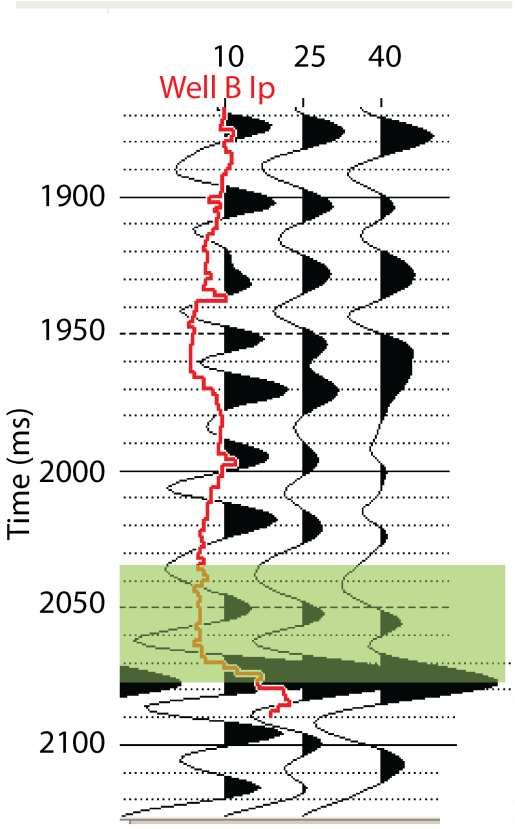

Figure 5.6: Example of super gather of near, mid, and far stacks around the angles 10, 25, and 40 degrees from crossline 1274 at inline 3622. The Haynesville is highlighted in green, and the Ip log from well B is superimposed.

Figure 5.7 shows an analysis of the 3D inversion at well B including from left to right the results for Ip, Is, density and Vp/Vs. The black line in these panels is the initial model, the blue is measured impedance, and the red is the inversion result at well B. The inversion matches the measured points in all four of these properties. The figure also displays the wavelet group of three wavelets used in the inversion, and a zero-offset synthetic calculated from the inversion results and these wavelets. This synthetic generated from the inverted model shows a correlation of .85 with the seismic trace from the location of well B.

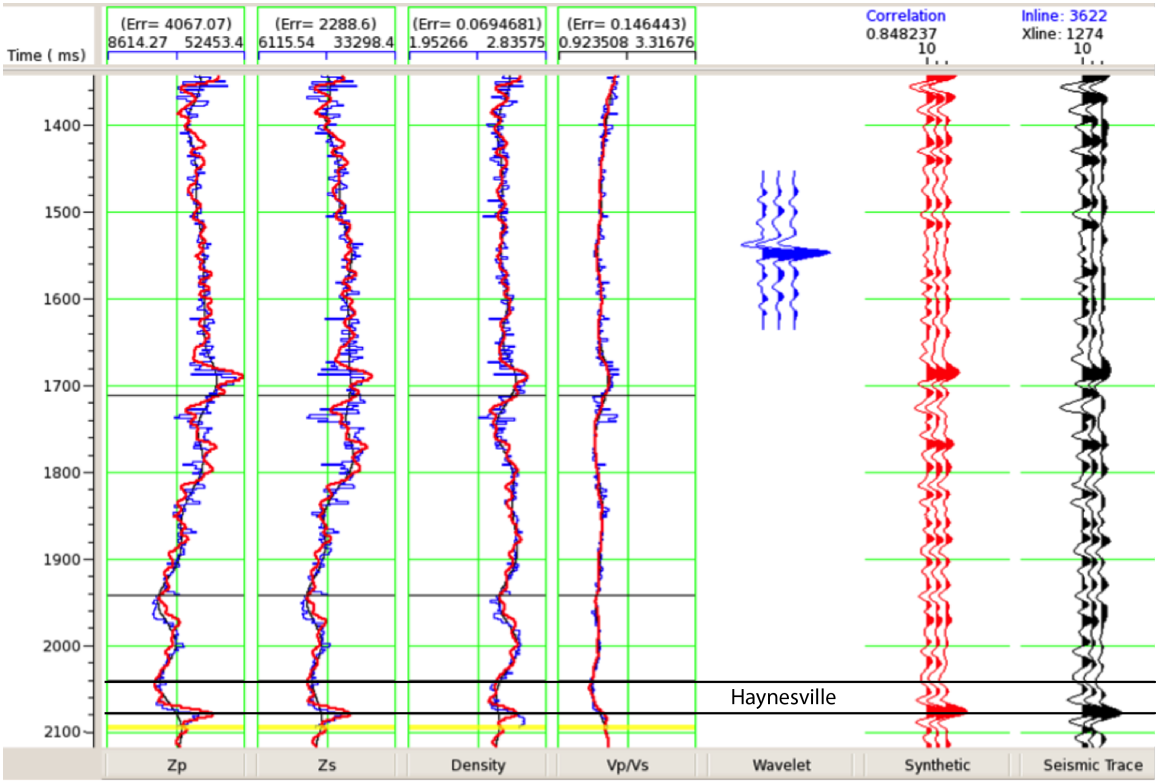

Figure 5.7: Analysis of the 3D inversion at well B showing from left to right the inversion results for Ip, Is, density and Vp/Vs. The black line in these panels is the initial model, the blue is measured impedance, and the red is the inversion result at well B. It also displays the group of three wavelets used in the inversion, a synthetic calculated from the inversion results and these wavelets, and the seismic traces from this well location. The top and base of the Haynesville are indicated by the black lines marked on the well panels.

Figure 5.8 shows an arbitrary profile through both wells in all three inverted volumes in time colored by amplitude of the inverted property. From left to right, the profile goes from northeast to southwest, with well A on the left and well B on the right. The top and base of the Haynesville are marked with bold black horizons. The wells are marked by black rectangles with the same properties measured at the well colored by the same scale. The inversion was trained at well B (on the right). The inversion results match the measured well data at the training well (well B on the right) and the test well

(well A on the left) in the Haynesville. The Haynesville shows higher P- and S-impedance and density at the top through most of the section, especially where the Haynesville extends deeper to the northeast. The high impedance and density of the Smackover below is evident in all three panels.

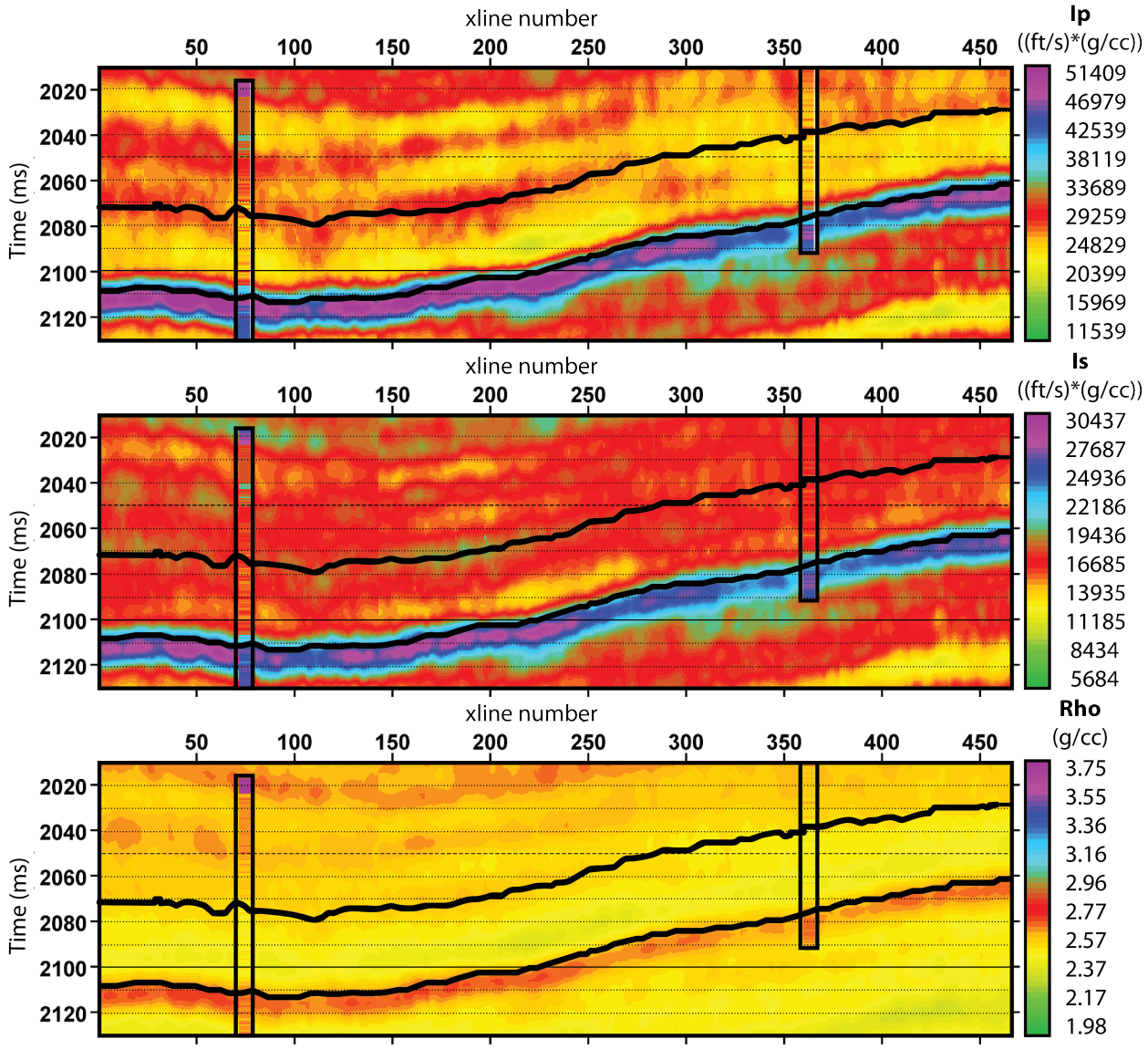

Figure 5.8: 3D inversion results. An arbitrary line section through both wells in all three inverted volumes in time colored by amplitude of the inverted property. Well A is marked on the left (northeast) with a black rectangle and colored by the same property as the arbitrary line and well B on the right (southwest). The top and base of the Haynesville are marked with bold black horizons.

5.2.2 Grid Searching

The elastic property volumes generated in the model-based inversion were then grid searched using the same workflow as the 1D inversion. The same prior distributions and modeling space were also used (figures 5.1 and 5.2). The objective functions, however, were modified to accept a larger range of models. Figure 5.9 shows the model space with the well measurements, the Backus averaged well measurements, and the Ip and Is inverted from the 3D seismic volume at well A. Because of the decreased resolution, the upscaled well measurements collapse to a tighter cluster. The inverted impedances and densities are effectively upscaled by the lower resolution of the seismic data. These data collapse to show less variation in Ip, Is, and density. The inverted data also show a shift to larger Is values relative to the well log and upscaled well log data. This shift is likely due in part to lower resolution; the Bossier and Smackover were sampled simultaneously with the top and base, respectively, of the Haynesville Shale. Both of these formations have larger Ip, Is, and density values than the Haynesville. The shift might also result from error in the inversion. Specifically, linear relationships between the logarithms of Ip, Is, and density were defined to constrain the inversion. These relationships were established using trends from the well logs, and error in this constraint would affect the inverted Ip and Is relationship. To account for the shift in the inverted values, the objective functions were modified as seen in equations 5.4 to 5.6.

$$Obj_P = \left| I_{P\,\mathrm{model}} - I_{Pinverted} \right| \leq 500 \tag{5.4}$$

$$Obj_S = \left| I_{S\,\mathrm{model}} - I_{Sinverted} \right| \leq 500 \tag{5.5}$$

$$Obj_\rho = \left| \rho_{\mathrm{model}} - \rho_{inverted} \right| \leq .5 \tag{5.6}$$

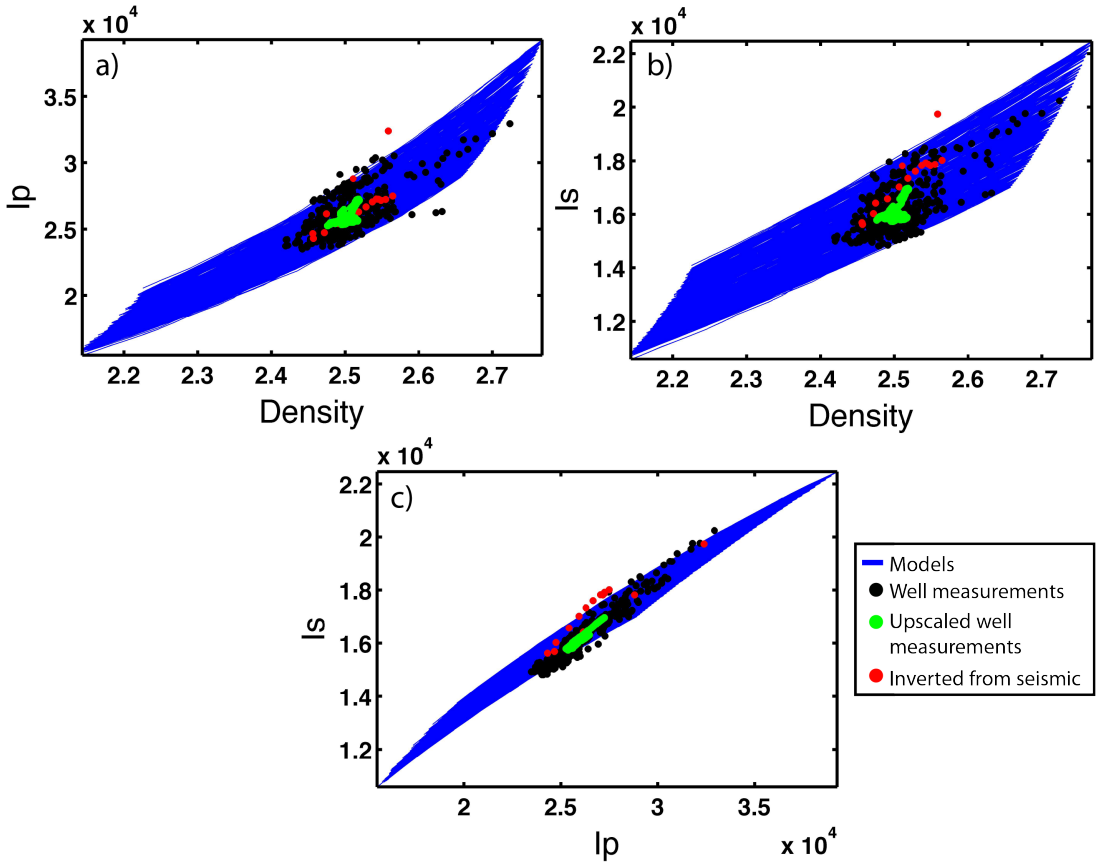

Figure 5.9: Models (blue lines) used in the inversion consisting of 10 iterations of 50 different mineral compositions over a given porosity range from 0 to 25 percent. a) and b) show density plotted against Ip and Is respectively, and c) shows Ip plotted against Is. Ip, Is, and density are the three properties constraining the objective functions for the rock physics inversion. Plotted with the model lines are the measured values from well A (black), upscaled (Backus averaged) measured values from well A (green) and inverted Ip, Is, and density from the 3D seismic volume at trace corresponding to well A.

5.2.3 3D Results and discussion

The 3D grid search was performed trace-by-trace, and the mean rock property (porosity or mineral composition) and the standard deviation for the models selected for

each trace and depth point were stored as new rock property volumes. The porosity volume and standard deviation in porosity are shown in figure 5.10. Hot colors represent high values of porosity while cold colors represent lower values. The top and base of the Haynesville are marked with bold black horizons. Black shaded areas indicates that the region is outside of the Haynesville Shale.

The porosity inversion results within the Haynesville predict consistently low porosity at the very base of the Haynesville throughout the entire profile. The highest porosity tends to occur in the mid to lower Haynesville in the northeast and in the upper Haynesville to the southwest. These values are the highest in the Haynesville up to about 14 percent. In general this shows a relatively larger porosity associated with lower Ip and Is observed in the inversion result.

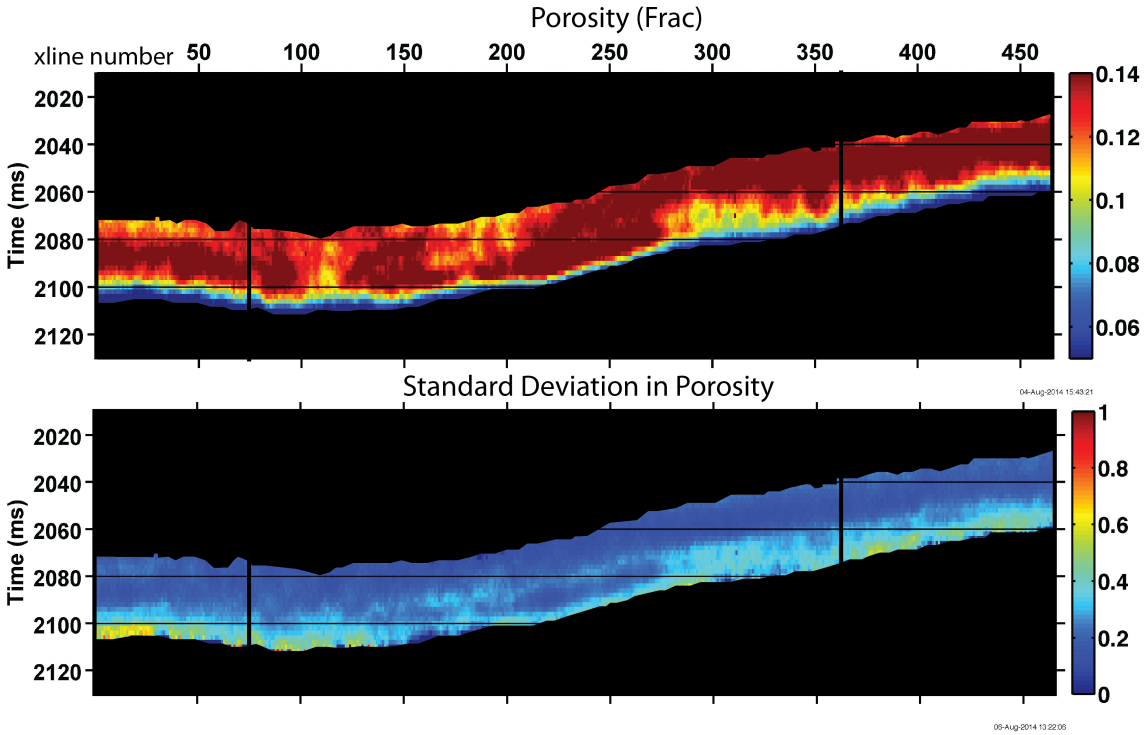

Figure 5.10: 3D rock property inversion results for porosity. An arbitrary line section through both wells in porosity and porosity standard deviation volumes. The standard deviation is normalized by dividing by the mean. Well A is marked on the left (northeast) with a vertical line and well B on the right (southwest). Black indicates that the region is outside of the Haynesville Shale.

The inversion estimates of composition include fractions of calcite, quartz, clay and kerogen. These results from the same arbitrary section are shown in that order in figure 5.10 with the associated standard deviations in figure 5.11. Again, the higher concentrations in all result panels are represented by hotter colors while the cooler colors indicate lower volumes of that mineral. The top and base of the Haynesville are marked with bold black horizons. Black indicates that the region is outside of the Haynesville Shale. The highest calcite concentrations are predicted in the upper half of the

Haynesville and at the very base of the Haynesville in contact with the underlying limestone. These relative concentrations are consistent with the mineralogical data observed in both wells and with the rock-type observations made in chapter 4. The carbonate percentage appears to decrease slightly from the northeast to the southwest. As with the 1D inversion, the clay and quartz results are identical in the 3D inversion based on the prior distributions allowed in the modeling space. Together they predict a higher concentration of siliciclastic material in the middle to lower Haynesville. This prediction is also consistent with the observations made from the mineralogical data and the rock-type descriptions of chapter 4. The kerogen volume is slightly lower in the more calcite rich upper Haynesville, but fairly consistent throughout the interval of interest.

In the regions with high calcite, the actual calcite volume is overpredicted when compared with well data and siliclastic fractions slightly over underpredicted. Well A measured values range from about 35-45 percent carbonate material in the upper Haynesville, while these inversion results describe about 40-50 percent. (Well B mineralogical measurements were not available for the upper Haynesville.) The opposite is true in the regions with high siliciclastic material. In these regions the siliclastic material is slightly overestimated again by about 5-10 percent at both wells. In both cases the model describes a slightly more extreme distribution of mineral content than what is observed with the higher frequency measurements at the wells.

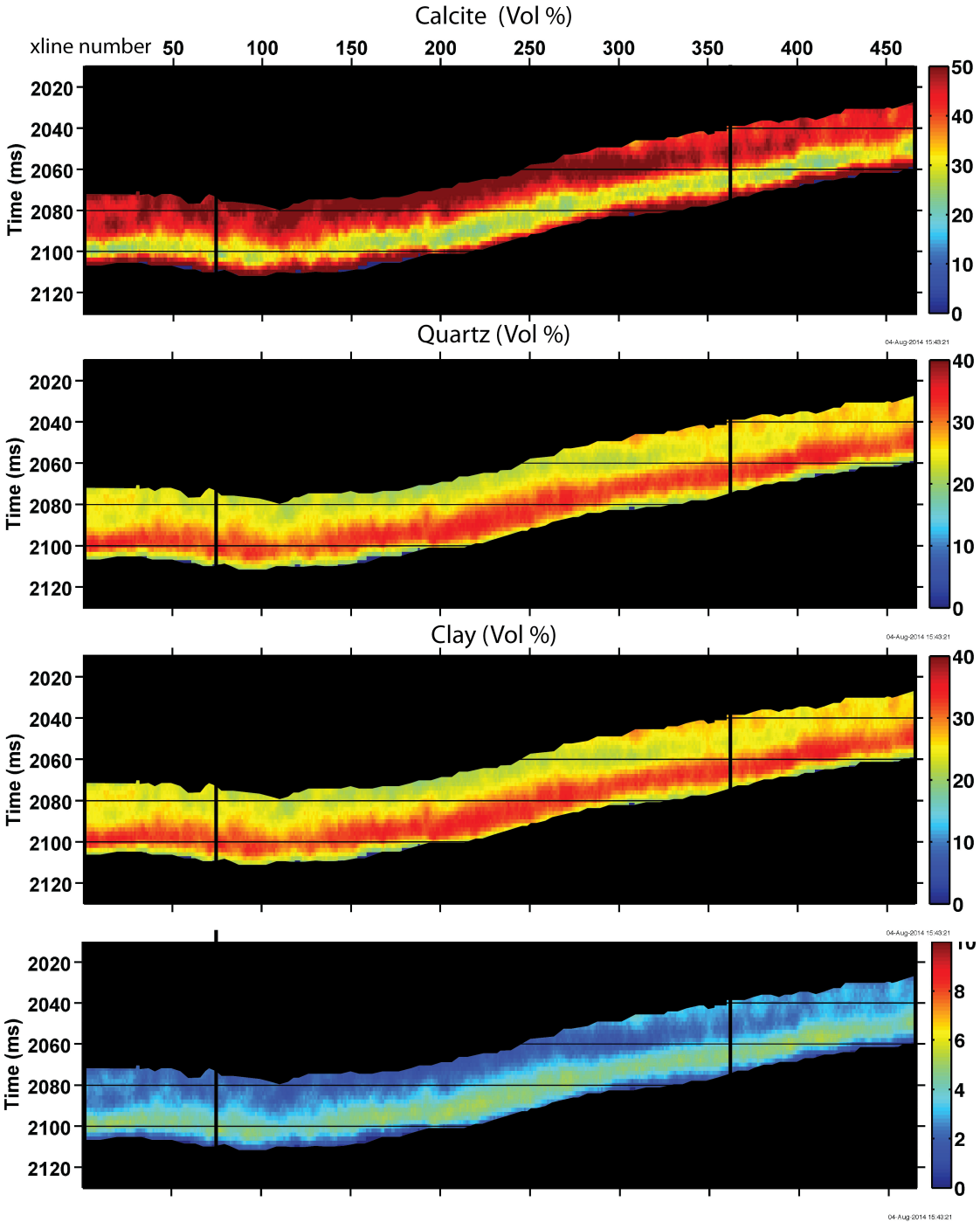

Figure 5.11 (caption on following page)

Figure 5.11: 3D rock property inversion results for mineral composition. An arbitrary line section through both wells in calcite, quartz, clay, and kerogen. Well A is marked on the left (northeast) with a vertical line and well B on the right (southwest). Black shaded regions indicates are outside of the Haynesville Shale.

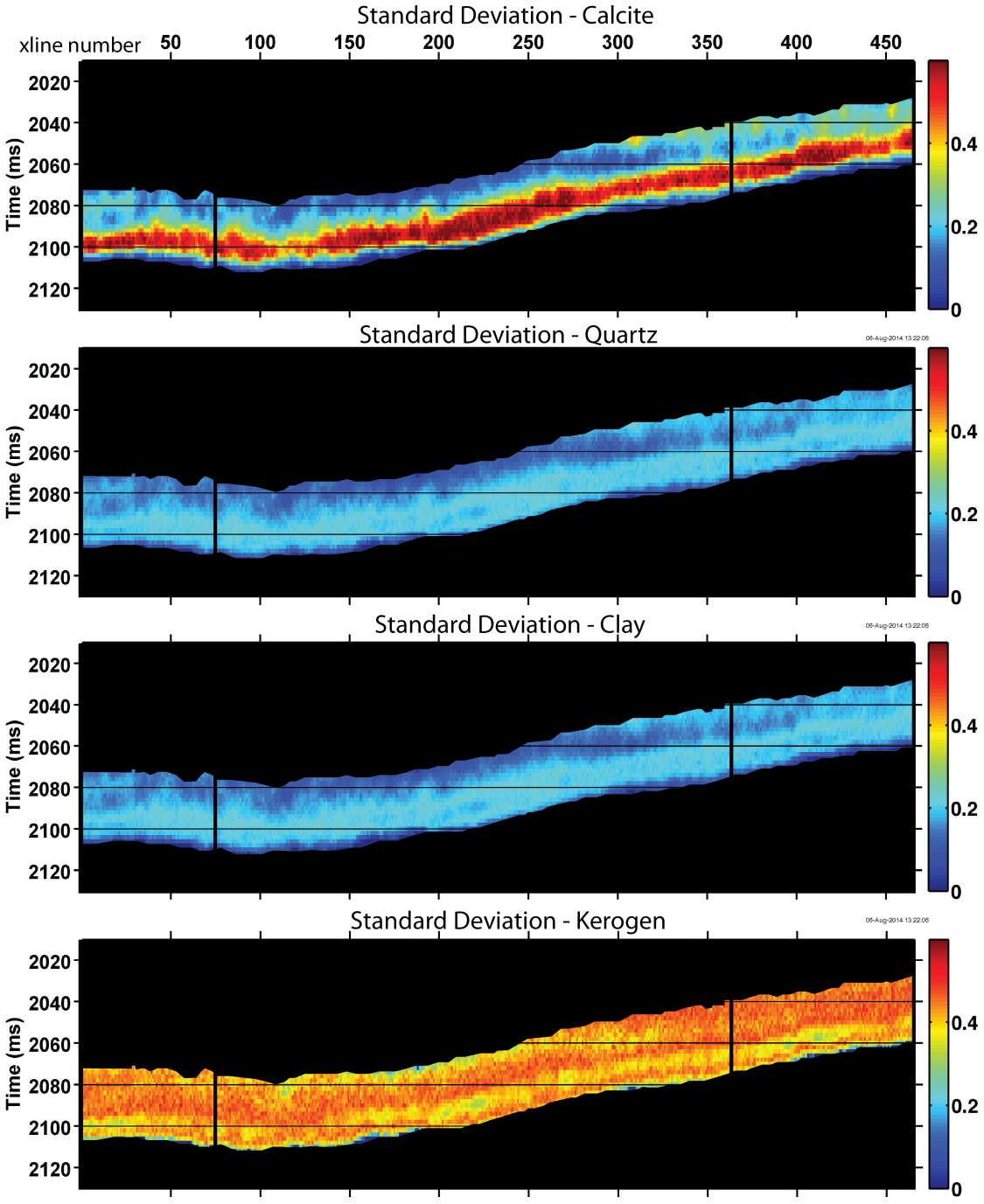

Figure 5.12 (caption on the following page)

Figure 5.12: The standard deviations in the 3D rock property inversion results from an arbitrary line section through both wells for mineral composition in calcite, quartz, clay, and kerogen. The standard deviations are normalized by dividing by the mean value at each depth point. Well A is marked on the left (northeast) with a vertical line and well B on the right (southwest). Black shaded regions are outside of the Haynesville Shale.

5.3 DISCUSSIONS AND CONCLUSIONS

Results from the 1D inversion show that the model built in chapter 4 combined with the grid-searching inversion workflow estimate porosity well and calcite and kerogen very well. However, the inability of the model space to represent a variation in quartz to clay ratio limited both the 1D and 3D inversions to a prediction of relative siliciclastic material. In the 3D inversion, a higher percentage of the dominant materials is reported by the inversion results in both high calcite and in high siliciclatic regions. This skewing of the inversion prediction may result from the prior distributions bias toward equivalent percentage of quartz and clay. By maintaining a constant ratio between the two in this inversion scheme, even though I add the minerals separately with distinct pore aspect ratios, stiffnesses, and densities, I am effectively modeling siliciclastics as a single mineral phase with averaged rock properties. However, the technique still provides a good description of the distribution of carbonate material and relative siliciclastic material, and also the regions with the highest organic content. By inverting the entire volume, a map of mineral content can provide the best areas for hydraulic fracturing and the highest porosity.

5.4 REFERENCES

Aki, K., and P. G. Richards, 2002, Quantitative Seismology, 2nd Edition: W. H. Freeman and Company.

Hampson, D. P., B. H. Russell, and B. Bankhead, 2005, Simultaneous inversion of prestack seismic data: 75th Annual International Meetings, SEG, Expanded Abstracts, 1633–1636.

Jiang, M., 2014, Seismic Reservoir Characterization of the Haynesville Shale: rock-physics modeling, prestack seismic inversion and grid searching, PhD thesis, The University of Texas at Austin.

Sen, M. and P. L. Stoffa, 1995, Global optimization methods in geophysical inversion: ELSEVIER Science.

Chapter 6: Conclusions and Future Work

6.1 Conclusions

This thesis investigated the relationship between elastic properties and rock properties of the Haynesville Shale using rock physics modeling, simultaneous seismic inversion, and grid searching. A workflow was developed in which a rock physics model was built and calibrated to well data in the Haynesville Shale and then applied to 3D seismic inversion data to predict porosity and composition away from the borehole locations.

In chapter 4, the rock physics model described the relationship between porosity, mineral composition, pore shape, and elastic stiffness using the anisotropic differential effective medium model. The sensitivity of the model to changes in rock fabric was investigated using two rock-type models: a calcite-rich and a clay- and silica-rich rock type. Rock-typing highlighted a steeper stiffness-porosity trend in the calcite-rich rock type than in the siliciclastic rich rock type. However, the changes in fabric within the Haynesville are below the sensitivity of the anisotropic differential effective medium model. A representative mean pore aspect ratio of 0.3 was instead calibrated for the entire interval of interest. Six idealized model lines were generated to describe the mineral composition's effect on the porosity-stiffness trend within the entire Haynesville Shale.

In chapter 5, the calibrated rock physics model was used to generate 12,500 realizations. This number represented 10 independent iterations calculated with pore aspect ratios drawn from a normal distribution and 50 distinct mineral assemblages at 25 porosity percentages. This modeling space was grid searched to provide a range of models at each depth point to invert both 1D well log data and 3D seismic data. The grid-searching inversion workflow estimated successfully the porosity trend and calcite and

kerogen volumes closely in the 1D inversion. However, the model space did not represent a variation in quartz to clay ratio, which limited both the 1D and 3D inversions to a prediction of the occurrence of the siliciclastic-rich rock type, rather than a description of the ratio between these two minerals within this rock-type. In the 3D inversion, the locations of calcite-rich rock type and siliciclastic rock type are predicted away from the borehole such that they can be mapped throughout the volume. The locations of areas of high or low porosity and of high or low kerogen content were mapped using this modeling technique and inversion workflow. This map of mineral content, kerogen, and porosity can be interpreted to predict the best areas for hydraulic fracturing. It also can provide a more detailed picture of the depositional environment in the area of interest by indicating regions of higher and lower carbonate input relative to siliciclastic material.

6.2 FUTURE WORK

In the grid searching technique, porosity, mineral assemblage, and pore aspect ratio are inverted for simultaneously. Resulting mineral and porosity volumes should be utilized together as a single likely solution to this under-determined and ill-posed problem. In the 3D inversion, the most likely models were selected based only on constraint by the objective functions. This rock physics inversion could be expanded to include information from the well logs in the 3D inversion such that proximity to a borehole with known mineral assemblage could help constrain the 3D solution. This geostatistical approach could allow for the use of a larger prior distribution of models and perhaps mapping of quartz and clay volumes independently. A more accurate estimate of these minerals will further improve the porosity, kerogen, and calcite estimates. With the

best possible estimate of kerogen and calcite, interpreters can better identify ideal locations with high calcite and large volume of organic content.

References

Aki, K., and P. G. Richards, 2002, Quantitative Seismology, 2nd Edition: W. H. Freeman and Company.

Auld, B.A., 1973, Acoustic fields and waves in solids, Vol. 1 and 2, John Wiley & Sons, Inc., New York.

Alzate, J. H., and D. Devegowda, 2013, Investigation of surface seismic, microseismic, and production logs for shale gas characterization: Methodology and field application: Interpretation, **1**, 37–49.

Avseth, P., T. Mukerji, G. Mavko, and J. Dvorkin, 2010, Rock-physics diagnostics of depositional texture, diagenetic alterations, and reservoir heterogeneity in high-porosity siliclastic sediments and rocks – A review of selected models and suggested work flows: Geophysics, **75**, 5, 75A31–75A47.

Bandyopadhyay, K., 2009, Seismic anisotropy: geological causes and its implications to reservoir geophysics: Ph.D. thesis, Stanford University.

Batzle, M., and Z. Wang,1992, Seismic properties of pore fluids: Geophysics, **57**, No. 11, 1396-1408.

Berryman, J. G., 1980, Long-wavelength propagation in composite elastic media: The Journal of the Acoustical Society of America, **68**, 1809–1831, doi: 10.1121/1.385171.

Budiansky, B., 1965, On the elastic moduli of some heterogeneous materials: Journal of the Mechanics and Physics of Solids, **13**, 223–227.

Buller, D., and M. C. Dix, 2009, Petrophysical evaluation ofthe Haynesville Shale in northwest Louisiana and northeast Texas: Gulf Coast Geological Association of Geological Societies Transactions, **59**, 127**–**143.

Chalmers, G. R., R. M. Bustin, and I. M. Power, 2012, Characterization of gas shale pore systems by porosimetry, pycnometry, surface area, and field emission scanningelectron microscopy/transmission electron microscopy image analyses: Examples from the Barnett, Woodford, Haynesville, Marcellus, and Doig units: AAPG Bulletin, **96**, 1099–1119, doi: 10.1306/10171111052.

Chapman, M., 2003, Frequency-dependent anisotropy due to meso-scale fractures in the presence of equant porosity: Geophysical Prospecting, **51**, 369–379.

Dræge, A., M. Jakobsen, and T. A. Johansen, 2006, Rock physics modeling of shale diagenesis: Petroleum Geoscience, **12**, no. 1, 49–57, doi: 10.1144/1354-079305-665.

Eshelby, J. D., 1957, The determination of the elastic field of an ellipsoidal inclusion and related problems: Proceedings of the Royal Society of London, Series A, **241**, 376-396.

Gabor, D., 1946, Theory of communication: J. IEEE (London), **93**(III), 429-457.

Gardner, G. H. F., L. W. Gardner, and A. R. Gregory, 1974, Formation velocity and density—The diagnostic basics for stratigraphic traps: Geophysics, **39**, 770–780, doi: 10.1190/1.1440465.

Greenberg, M. L., and J. P. Castagna, 1992, Shear-wave velocity estimation in porous rocks: Theoretical formulation, preliminary verification and applications: Geophysical Prospecting: **40**, 2, 195–209, doi: 10.1111/j.1365-2478.1992.tb00371.x.

Hammes, U., H. S. Hamlin, and R. Eastwood, 2010, Facies characteristics, depositional environments, and petrophysical characteristics of the Haynesville and Bossier shale gas plays of east Texas and northwest Louisiana: Houston Geological Society Bulletin, May 2010, 59-63.

Hammes, U., H. S. Hamlin, and T. E. Ewing, 2011, Geologic analysis of the Upper Jurassic Haynesville Shale in east Texas and west Louisiana: AAPG Bulletin, **95**, 10, 1643–1666.

Hampson, D. P., B. H. Russell, and B. Bankhead, 2005, Simultaneous inversion of prestack seismic data: 75th Annual International Meetings, SEG, Expanded Abstracts, 1633–1636.

Han, D., 1986, Effects of porosity and clay content on acoustic properties of sandstones and unconsolidated sediments: Ph.D. dissertation, Stanford University.

Hashin, Z., and S. Shtrikman, 1963, A variational approach to the elastic behavior of multiphase materials: Journal of the Mechanics and Physics of Solids, **11**, 2, 127–140, doi: 10.1016/0022-5096_63_90060-7.

Haynesville-Bossier Shale Play, Texas-Louisiana Salt Basin. 26 May 2011. Web. 1 Aug. 2013. <http://www.eia.gov/oil_gas/rpd/shaleusa4.pdf>.

Hill, R., 1965, A self-consistent mechanics of composite materials: Journal of the Mechanics and Physics of Solids, **13**, 213–222.

Hornby, B., L. M. Schwartz, and J. A. Hudson, 1994, Anisotropic effective–medium modeling of the elastic properties of shales: Geophysics, 59, 1570–1583.

Horne, S., J. Walsh, and D. Miller, 2012, Elastic anisotropy in the Haynesville Shale from dipole sonic data: First Break, **30**, 37–41.

Jiang, M., 2014, Seismic Reservoir Characterization of the Haynesville Shale: rock-physics modeling, prestack seismic inversion and grid searching: PhD thesis, The University of Texas at Austin.

Kumar, V., C. H. Sondergeld, and C. S. Rai, 2012, Nano to macro mechanical characterization of shale: Annual Technical Conference and Exhibition, SPE, Paper SPE 159808-PP.

Kuster, G. T., and M. N. Toksöz, 1974, Velocity and attenuation of seismic waves in two-phase media, Part I: Theoretical formulations: Geophysics, **39**, 587–606, doi: 10.1190/1.1440450.

Mavko, G., T. Mukerji, and J. Dvorkin, 2009, The Rock Physics Handbook: Tools for Seismic Analysis of Porous Media: Cambridge, University Press.

Mindlin, R. D., 1949, Compliance of elastic bodies in contact: Journal of Applied Mechanics, **16**, 259–268.

Montaut, A., 2012, Detection and quantification of rock physics properties for improved hydraulic fracturing in hydrocarbon-bearing shales: M.S. Thesis, The University of Texas at Austin.

Mura, T., 1982, Micromechanics of Defects in Solid: Martinus Nijhoff Pub.

Rickman, R., M. Mullen, E. Petre, B. Grieser, and D. Kundert, 2008, A practical use of shale petrophysics for stimulation design optimization: All shale plays are not clones of the Barnett Shale: Annual Technical Conference and Exhibition, Society of Petroleum Engineers, SPE 11528.

Rüger, A., 2002, Reflection coefficients and azimuthal AVO analysis in anisotropic media: Society of Exploration GeophysicsMonograph Series.

Ruud, B., M. Jakobsen, and T. A. Johansen, 2003, Seismic properties of shales during compaction: 73rd Annual International Meeting, SEG, Expanded Abstracts, 1294–1297, doi: 10.1190/1.1817522.

Sen, M. and P. L. Stoffa, 1995, Global optimization methods in geophysical inversion: ELSEVIER Science.

Spath, Helmuth. The cluster dissection and analysis theory fortran programs examples, Prentice-Hall, Inc., 1985.

Tatham, R.H. and McCormack, M.D., 1991, Multicomponent seismology in petroleum exploration: Investigation in Geophysics Series, **6,** Society of Exploration Geophysicists.

Tatham, R.H., Matthews, M.D., Sekharan, K.K., Wade, C.J., and Liro, L.M., 1992, A physical model study of shear-wave splitting and fracture intensity: Geophysics, **57**, No. 20, p. 647-652.

Thomsen, L., 1986, Weak elastic anisotropy: Geophysics, **51**, 1954–1966, doi: 10.1190/1.1442051.

Vernik, L., and C., Landis, 1996, Elastic anisotropy of source rocks: Implication for hydrocarbon generation and primary migration: AAPG Bulletin, **80**, 531–544.

Wang, F. P., and U. Hammes, 2010, Effects of reservoir factors on Haynesville fluid flow and production: World Oil, **231**, D3–D6.

Wu, T. T., 1966, The effect of inclusion shape on the elastic moduli of a two-phase material: International Journal of Solids and Structure, **2**, 1-8.

Zhang, K., B. Zhang, J. T. Kwiatkowski, and K. J. Marfurt, 2010, Seismic azimuthal impedance anisotropy in the Barnett Shale: 80th Annual International Meeting, SEG, Expanded Abstracts, 273–277.

Vita

Sarah Coyle attended the University of Texas at Austin where she earned a Bachelor of Science in Geological Sciences (Option II: Geophysics) in 2012. After graduating, she remained at UT Austin and joined the Master of Science program at the Jackson School of Geosciences to study exploration geophysics. She completed an internship at ExxonMobil in the summer of 2013, and will start work at Chevron after graduation in 2014.

Email: sarahcoyle@utexas.edu

This thesis was typed by Sarah Coyle.